Published in final edited form as:

Neurobiol Aging. 2015 September ; 36(9): 2483–2500. doi:10.1016/j.neurobiolaging.2015.05.022.

Activated iron-containing microglia in the human hippocampus identified by magnetic resonance imaging in Alzheimer disease

Michael M. Zeineh[a,*], **Yuanxin Chen**[b], **Hagen H. Kitzler**[c], **Robert Hammond**[d], **Hannes Vogel**[e], and **Brian K. Rutt**[a]

[a]Department of Radiology, Lucas Center for Imaging, Stanford University, Stanford, CA, USA

[b]Imaging Research Laboratories, Robarts Research Institute, Western University, London, Ontario, Canada

[c]Department of Neuroradiology, University Hospital Carl Gustav Carus, Technische Universität Dresden Dresden, Germany

[d]Department of Pathology and Clinical Neurological Sciences, Schulich School of Medicine and Dentistry, Western University, London, Ontario, Canada

[e]Department of Pathology, Stanford University, Stanford, CA, USA

Abstract

Although amyloid plaques and neurofibrillary pathology play important roles in Alzheimer disease (AD), our understanding of AD is incomplete, and the contribution of microglia and iron to neurodegeneration is unknown. High-field magnetic resonance imaging (MRI) is exquisitely sensitive to microscopic iron. To explore iron-associated neuroinflammatory AD pathology, we studied AD and control human brain specimens by (1) performing ultra-high resolution ex vivo 7 Tesla MRI, (2) coregistering the MRI with successive histologic staining for iron, microglia, amyloid beta, and tau, and (3) quantifying the relationship between magnetic resonance signal intensity and histological staining. In AD, we identified numerous small MR hypointensities primarily within the subiculum that were best explained by the combination of microscopic iron and activated microglia ($p = 0.025$), in contradistinction to the relatively lesser contribution of tau or amyloid. Neuropathologically, this suggests that microglial-mediated neurodegeneration may occur in the hippocampal formation in AD and is detectable by ultra-high resolution MRI.

Keywords

Hippocampus; Microglia; Iron; Alzheimer; MRI; Amyloid

---

[*]Corresponding author at: Department of Radiology, Stanford University, Lucas Center for Imaging, Rm. P271, 1201 Welch Road, Stanford, CA 94305-5488. Tel.: 650 721 1419; fax: 650 723 5795. mzeineh@stanford.edu (M.M. Zeineh).

Disclosure statement

The authors have no other conflicts of interest to disclose.

Appendix A. Supplementary data

Supplementary data associated with this article can be found, in the online version, at http://dx.doi.org/10.1016/j.neurobiolaging.2015.05.022.

1. Introduction

Alzheimer disease (AD) is pathologically characterized primarily by the presence of amyloid beta (Aβ) plaques and tau-rich neurofibrillary tangles in the clinical context of memory impairment (Braak and Braak, 1991; Selkoe, 2008). Although Aβ has a strong genetic link to AD (Tanzi, 2012), the mechanism of plaque-mediated neurodegeneration is unclear because of the presence of plaques in healthy elderly controls (Arnold et al., 2013; Davis et al., 1999) and the lack of a strong correlation between plaque deposition and the severity of dementia (Terry et al.,1991). Neurofibrillary tangles have a strong correlation with mnemonic impairment, but the genetics of tau mutations are associated with other neurodegenerative disorders (Goedert and Jakes, 2005), and the mechanism of tau pathogenesis and relationship to Aβ is unclear (Spires-Jones and Hyman, 2014). In comparison to amyloid plaques, soluble Aβ oligomers have a stronger correlation with clinical complaints (Tomic et al., 2009). Aβ in vitro has been shown to convert the redoxinactive ferric iron (Fe^{3+}), normally present in the storage form of iron (ferrihydrite), to the redox-active ferrous (Fe^{2+}) iron, a catalyst of the Fenton reaction that generates toxic free radicals, a driver of inflammation (Everett et al. 2014a, 2014b). This in vitro result is relevant because abnormal iron accumulation occurs in AD (Lovell et al., 1998; Smith et al., 1997), and rather than being mineralized as the typical storage form of Fe^{3+} within ferrihydrite, it is more composed of magnetite and wüstite, which both possess Fe^{2+} (Collingwood et al., 2008; Pankhurst et al., 2008; Quintana et al., 2004). The broader neuroinflammation literature in AD has shown colocalization of microglia (the inflammatory cells of the nervous system) with sites of AD pathology including the medial temporal lobe (Sheng et al., 1995) and colocalization of ferritin (which stores intracellular iron) with microglia in AD (Connor et al., 1992; Grundke-Iqbal et al., 1990). A genome-wide expression study found a 10-fold gain-of-function in AD of microglial gene networks, and this gene network had the strongest correlation of all gene modules with AD neuropathology (Zhang et al., 2013). Microglial cell-surface antigen CD33 expression is elevated in AD and inversely correlated with plaque clearance (Gandy and Heppner, 2013; Griciuc et al., 2013). A murine model of AD incorporating an altered immune-redox state recapitulates the pathological progression of amyloid, tau, and neuronal loss seen in humans better than other mouse models (Colton et al., 2014). Thus, iron-associated microglial-driven neuroinflammation may be a significant driver behind neuronal destruction, synergistic with amyloid (Gallagher et al., 2012; McGeer and McGeer, 2013). However, no study to date has quantified or even identified the distribution of iron-containing microglia in the medial temporal lobe or described the relationship of these microglia to both amyloid and tau deposition.

High-field magnetic resonance imaging (MRI) is exquisitely sensitive to microscopic iron and can be performed at ultra-high resolution ex vivo. However, all ex vivo MRI work in AD has focused exclusively on Aβ plaques. Although initial efforts at plaque visualization reported contradictory results (Benveniste et al., 1999; Dhenain et al., 2002), later work using murine and human specimens definitively visualized iron associated with plaques in the entorhinal cortex (the hippocampus was not specifically depicted and microglia not assessed) (Meadowcroft et al., 2009).

In this study, we hypothesize that foci of hypointense signal on MR in AD would reflect iron deposits, and these deposits would be within activated microglia rather than Aβ plaques, reflective of an inflammatory component of AD. We imaged 5 AD and 5 control human hippocampal specimens with 7T MRI at ultra-high resolution (0.1mmisotropic) using 2 iron-sensitive pulse sequences. To discern the histological correlate underlying MR hypointensity, we sectioned the same specimens and performed successive triple staining using DAB (3,3’-diaminobenzidine tetrahydrochloride) enhanced Perl’s stain for iron, CD 163 for microglia, and an immunostain for Aβ. These stains were separable in the same section by color subtraction and coregistered with each other and the MRI. We additionally employed phospho-tau-AT8 immunostaining on adjacent sections to explore the relationship with neurofibrillary pathology. Finally, we delineated the exact location of these MR hypointense foci with regard to hippocampal subfields by performing and coregistering anatomic Nissl, myelin, and acetylcholinesterase (AChE) stains.

2. Methods

2.1. Overview of methodology

Five 4-mm thick slabs from fixed human AD and control specimens (Table 1) were placed in a container and supported by thin plastic sheets (Fig. 1A). The container fit tightly within a solenoidal coil to minimize the distance between the coil and the tissue, thereby optimizing signal sensitivity and image quality (Fig. 1B and C). Slabs were then paraffin-embedded and sectioned at 10-μm thickness in their entirety. Every 30th section was double-stained with DAB-iron and CD163, and the entire slide was scanned at low resolution with bright-field microscopy to form a low-resolution histologic volume to aid in alignment (Fig. 1D). Adjacent to 1 of these double-stained sections, a near-contiguous set of 5 sections spaced over approximately 100 μm (the thickness of an MR voxel) was serially stained with iron, microglia, and Aβ. After each successive stain the entire slide was scanned at high resolution to form a high-resolution, successively stained histologic volume consisting of single (DAB-iron), double (DAB-iron and CD163), and triple (DAB-iron, CD163, and Aβ) stains (Fig. 2A, top row). Registration of all of the histological sections to each other permitted construction of a combined low and high-resolution histological volume (Fig. 1D and E). Using a fiducial-based nonlinear alignment procedure, this histologic volume was then coregistered to the MRI, achieving a precise overlap of hippocampal subfields and the adjacent parahippocampal gyrus (Fig. 1F). To separate the successive stains into separate images of iron, microglia, and Aβ, the high-resolution scanned successive single, double, and triple stains were tightly coregistered, and digital subtraction was performed of the single stain from the double stain, and the double stain from the triple stain (Fig. 2A and C). Individual stains were then segmented based on image intensity (Fig. 2B and C). High-pass filtering was applied to the MR to extract the small hypointense foci (Fig. 2D, top row, middle column). To compare the spatial distributions of the histology stains with that of the MR hypointense foci, we used histogram binning and image resizing to create quantitative density maps indicative of the distribution of the segmented histology stains and high-pass filtered MR images, respectively (Fig. 2D). Regions of artifacts, tissue edges, and large vessels and/or perivascular spaces (tubular structures on serial MR images) were manually masked out (red in Fig. 2D). The quantitative histology armamentarium was completed by staining for phosphotau-AT8 separately on an adjacent section, aligning the scanned slide into the high-resolution histological volume, and segmenting in a similar manner. The critical border between the hippocampal CA fields and subiculum was delineated using visual inspection of coregistered Nissl, AChE, and myelin stains (Fig. 3).

After established anatomic terminology of the medial temporal lobe (Witter and Amaral, 1991), we use proximal and/or distal to refer to nearer and/or farther from the dentate gyrus (e.g., CA1 is proximal to the subiculum, and the subiculum is distal to CA1), and superficial and/or deep refers to nearer and/or farther from the hippocampal sulcus (e.g., the molecular subiculum is superficial to the subicular pyramidal layer).

2.2. Detailed methodology

2.2.1. Specimen MRI—Five AD (A1–A5) and 8 normal control (N1–N8) formalin-fixed human brain specimens were obtained from neuropathology (Table 1). Each specimen consisted of 3-cmby 3-cmsquare by 4-mm thick slabs from the frontal lobe, parietal lobe, medial temporal lobe, superior temporal gyrus, and occipital lobe. These sections from specimens A1–A5 and N1–N5 were separated by a thin plastic sheet and immersed in Fluorinert (3M, USA) in a 4-cm diameter sealed container within a scaffold to ensure nomotion (Fig.1A).MR imaging was performed using a 2-cm long transmit and/or receive radiofrequency solenoid coil (Fig. 1B) at 7T (GE/Agilent Discovery MR901). We used a modified balanced steady-state free precession sequence (bSSFP) for all imaged specimens as well as a gradient echo (GRE) sequence for A1–A5 and N4 (coronal 3D bSSFP or GRE acquisition, repetition time 21, echo time 10.5, flip angle 20, phase cycles 8 for bSSFP, number of excitations 8 for GRE, 0.1-mm isotropic voxels, field-of-view (FOV) 3 cm, 256 slices, bandwidth 8 kHz, total scan time 3 hours 37 minutes each, Fig.1C). Both sequences are highly and similarly iron sensitive. All the images were acquired at 0.1-mm isotropic voxel size and reconstructed at 0.0586 × 0.0586 in-plane with 0.1-mm slice thickness using a standard reconstruction.

2.2.2. Histologic sectioning and microscopy—All the AD and control hippocampal specimens were paraffin embedded and sectioned with a microtome at 10-μm thickness. Occasional slides that were heavily distorted during the sectioning were discarded. Attempts at using immunofluorescence staining were hampered by extensive background signal related to lipofuscin autofluorescence. Instead, we pursued an approach of bright-field microscopy with successive, serial triple staining to visualize separately iron, microglia, and amyloid stains. Because tau was also of pathological interest, interleaved sections were single-stained for phospho-tau-AT8. Specimens from the remainder of the brain will be the subject of future studies and were not examined further here.

The slides were scanned using an Olympus Fv10i microscope at 10× resolution with a square pixel size of 0.68 μm and a rectangular image size of approximately 20,000 pixels, adjusted along each axis to cover the entire hippocampus and parahippocampal gyrus. Because of microscopy constraints, this image of the full specimen slide was acquired in 2–3 separate smaller FOV acquisitions for A4 and A5, which were merged into 1 composite image using the Fiji (http://fiji.sc/Fiji, (Schindelin et al., 2012)) plugin pairwise stitching

(Preibisch et al., 2009). A1–A3 and all control specimens were scanned in 1 contiguous FOV after a memory upgrade to the microscope.

2.2.3. Selection of slices for staining—For medial temporal lobes from 4 specimens (A1–A4), the entire 4-mm slab was double-stained with DAB-iron and/or CD163 every 30th slide and the entire slide was scanned at low resolution (300 × 400 pixels), and this composed a low-resolution histological volume suitable for rough alignment with the MRI (Fig. 1D). We estimated the ease of aligning portions of the low-resolution histological volume with MRI by the presence of similar landmarks (e.g., blood vessels and tissue edges), and then picked a set of 9 contiguous slices for staining procedures adjacent to the low-resolution histological image with the most conspicuous landmarks. The odd number sections (e.g., 1, 3, 5, 7, 9) underwent the triple staining and separation procedure described in 2.2.5, and 1 even numbered section underwent the phospho-tau single staining. On one of these specimens (A3), the 1st odd-numbered slice was discarded due to artifact. For 1 specimen (A5), a set of 11 contiguous sections was selected from the middle of the 4-mm slab. Instead of interleaved staining, 10 of these sections were triple-stained, 1 slide at the end was stained with phospho-tau, and approximately 5 slides were available on either side of these 11 sections for composing a low-resolution histological volume. At the end of this procedure, for each specimen there was a low-resolution histological volume encompassing at least half of the 4-mm slab, and a high-resolution histological volume composed of 6–11 near-contiguous slices. These 2 volumes were combined into a single histological volume for alignment, spacing the slices according to their section number.

For all control medial temporal lobe specimens, 2 slices were selected from the center of the slab, 1 for triple staining and the other for phospho-tau single staining.

For identification of the boundary between hippocampal subfield CA1 and the subiculum, 3 slides were selected adjacent to the center slice of each high-resolution volume for cresyl-violet Nissl staining, myelin staining, and AChE staining.

The selected sections were deparaffinized in 2 changes of xylene for 5 minutes each. Slides were then transferred to 100% alcohol for 2 changes, 3 minutes each and once through 95%, 70%, and 50% alcohols, respectively for 3 minutes each.

2.2.4. Single staining procedure—For all single-stain immunostains (phospho-tau-AT8, AChE, myelin) endogenous peroxidase activity was blocked by incubating sections in 3% H_2O_2 and 10% methanol solution at room temperature for 10 minutes. Slides were then rinsed for 2 changes in 300mL of tris-buffered saline (TBS) for 5 minutes each. Immunostaining for phospho-tau-AT8 was performed using an anti-human paired helical filaments-tau monoclonal antibody (10 μg/mL, MN1020, Pierce Biotechnology, Rockford, IL 61105, USA). For AChE, immunostaining was performed using an anti-AChE monoclonal antibody (1:100 dilution; product number: NB 300–528, Novus Biologicals, Canada). For myelin staining, immunostaining was performed using anti-human myelin basic protein monoclonal antibody, SMI94 (1:1000 dilution; AB24567, Abcam Inc). Slides were firstly incubated for 30 minutes in blocking reagent (15% horse serum in TBS) and rinsed 3 changes in TBS for 5 minutes each. Slides were then incubated with the primary antibody for 24 hours at 4 °C and rinsed 3 changes in TBS for 5 minutes each. Slides were incubated with horse anti-mouse biotinylated secondary antibody for 30 minutes at room temperature (1:300 dilution; BA2000, Vector Laboratories, Burlington, ON, USA) and rinsed in TBS for 3 changes, 5 minutes each. Tissue sections were processed using the (avidin-biotin complex) solution for 45 minutes (PK 4000, Vector Laboratories), rinsed for 3 changes in TBS for 5 minutes each, and incubated in DAB (0.5 mg/mL; SK4100, Vector Laboratories) for 30–60 seconds. Slides were dehydrated through 70%, 95%, and 100% alcohol for 3 minutes each, cleared 2 changes of xylene for 5 minutes each, and cover slipped for microscopic examination.

For the cresyl-violet Nissl stain, slides were incubated in 1% cresyl violet solution for 15 minutes. Slides were cleared in 1% acetic acid for 1 minute and rinsed in tap water for 5 minutes to remove excess stain. Slides was washed in 70% ethanol for 1 minute, dehydrated through 2 × 3 minutes changes of absolute ethanol, cleared in 2 changes of xylene for 5 minutes each, and coverslipped.

2.2.5. Triple stain successive-staining procedure—The tissue sections were first subjected to DAB-intensified Prussian blue that stains iron as dark brown. The slides were placed in equal volumes of freshly prepared 4% potassium ferrocyanide (P236, Fisher Scientific, Waltham, MA, USA) and 4% hydrochloric acid for 20 minutes at 37 °C and followed by 2 rinses in dH_2O. Intensification was performed with 3 minutes of DAB staining (D5637, Sigma, St. Louis, MO, USA; 10 mg dissolved in 15 mL of TBS with 16 μL of 30% H_2O_2) followed by 2 × 5 minutes of rinses in dH_2O. Sections were coverslipped with aqueous mounting medium and high-resolution digital microscopy performed.

Afterward, a CD163 antibody was employed on the same section, which stains all microglia as blue. Tissue sections were first immersed in the preheated (95 °C–100 °C) 0.01-M sodium citrate buffer (pH 6.0) in steam water bath for 30 minutes for antigen unmasking. The sections were allowed to cool for 20 minutes in the citrate buffer, then washed in TBS for 2 × 5 minutes and incubated for 30 minutes in blocking reagent (15% horse serum in TBS). Sections were incubated in the 1:100 dilution of mouse anti-human CD163 antibody (NCL-CD163, Leica Biosystems Newcastle Ltd, Newcastle Upon Tyne, UK) for 24 hours at 4 °C and rinsed 3 changes in TBS for 5 minutes each. Slides were incubated in 1:300 dilution of horse anti-mouse biotinylated secondary antibody for 30 minutes (BA2000, Vector Laboratories) and rinsed in TBS for 3 × 5 minutes. Tissue sections were processed using the ABC-AP solution for 30 minutes (Ak 5200, Vector Laboratories), rinsed 3 changes in TBS for 5 minutes each, and incubated in Vector Blue alkaline phosphatase substrate solution (SK-5300, Vector Laboratories) for 25 minutes in the dark. Slides were washed in TBS for 2 × 5 minutes, rinsed in water, and coverslipped with aqueous mounting medium for high-resolution digital microscopic examination.

Finally, an Aβ immune stain (Millipore) was added to the same section, which colored all the Aβ bright red. The tissue sections were immerged in 95%–98% formic acid (F0507, Sigma-Aldrich, Sigma-Aldrich Canada Co Oakville, ON, USA) for 10 minutes for antigen unmasking. The sections were washed in TBS buffer for 2 × 5 minutes and incubated for 30 minutes in blocking reagent (15% horse serum in TBS). Tissue sections were then incubated in the monoclonal mouse anti-human Aβ antibody (M0872, Dako Canada, Inc, Burlington, ON, USA) with a 1:200 dilution for 1 hour at room temperature. After rinsed 3 changes in TBS for 5 minutes each, sections were incubated with 1:100 dilution of alkaline phosphatase horse anti-mouse second antibody for 1 hour (AP2000, Vector Laboratories). The sections were finally incubated in Vector Red alkaline phosphatase substrate solution (SK-5100, Vector Laboratories) for 30 minutes. Slides were washed in TBS for 2 × 5 minutes, rinsed in water, and coverslipped with aqueous mounting medium for high-resolution digital microscopic examination.

To separate the 3 stains within a single histologic section, an extremely high-fidelity image registration is required between the single, double, and triple stains. We have addressed this challenge with a 2-stage registration procedure (Fig. 2A). First, the 3 stains within a slice were roughly coregistered using the Fiji linear SIFT plugin (http://fiji.sc/Linear_Stack_Alignment_with_SIFT). Then, an extremely precise registration was achieved between stains using a b-spline warping plugin to Fiji called bUnwarpJ (https://sites.google.com/site/iargandacarreras/software). The DAB-iron and CD163 double stain served as the target stain, and we created a separate background mask for each image using ImageJ's magic wand function to minimize excessive warping near tissue edges. Because bUnwarpJ empirically works optimally for images of on the order of 1000 × 1000 pixels, we used a python script to parcellate each histological image into 1400 × 1400 pixel overlapping tiles, with 200 pixels of overlap between adjacent tiles. After each of these 15 × 15 tiles were then piped to the bUnwarpJ plugin, a composite aligned image was reconstructed. Setting the divergence and curl weights to 0.5 prevented dramatic shrinkage or expansion of portions of the image. The initial deformation was set to fine, and final deformation set to super fine.

After this precise registration was achieved within slice and a common background mask employed, the CD163 stain was calculated by subtracting the single stain from the DAB-iron and CD163 double stains. Log-transformation was employed before and after subtraction to operate in units of optical density. A similar procedure was employed to subtract DAB-iron and CD163 from DAB-iron, CD163, and Aβ to deliver an image of Aβ.

2.2.6. Staining to define hippocampal subfield boundaries—To identify the location of iron deposits with respect to hippocampal subfields, we also performed the following stains on AD specimens 1, 3–5 and on the normal control specimens N6–8: cresylviolet Nissl staining, myelin staining, and AChE staining (Fig. 3).

To identify the key location of the prosubiculum, the cell field between the subiculum and CA1, we used the following criteria: (1) higher cell density and smaller cell size on Nissl staining of the prosubiculum when compared with CA1, (2) presence of the cell-sparse radiatum layer in CA1 but not in the prosubiculum (asterisk in Fig. 3), (3) in the prosubiculum there is a gradual increase of myelin extending from the deep and proximal prosubiculum pyramidal cell layer to the superficial and distal prosubiculum pyramidal cell layer; this forms the appearance of an oblique wedge (Fig. 3, blue curve), and (4) there is increased presubicular AChE staining (Ding, 2013; Rosene and Van Hoesen, 1987).

2.2.7. Composition of a histological volume—Serial histologic sections demonstrate minor distortions on successive slices, so an automated alignment was difficult to achieve. Instead, approximately 10–20 landmarks were chosen that could be followed through slice on both the low-resolution and high-resolution histological sections (Fig. 1E). The DAB-iron and CD163 double stain was chosen because this provided adequate visualization of tissue landmarks (vessels, perivascular spaces, tissue edges, and the gray-white junction), whereas the DAB-iron stain on its own did not have strong visibility of landmarks, and extensive amyloid staining on the triple stain obscured visualization of these landmarks. No specific pathologic features of the DABiron and CD163 double stain were selected (i.e., we did not align foci of iron deposition with microglia). A linear transformation (2D shifting, rotation, and isotropic scaling) was used to transform the low-resolution images to the high-resolution space. On the serial high-resolution sections, a nonlinear warping was performed using Fiji's Landmark Correspondence function (http://fiji.sc/Landmark_Correspondences) with a moving least squares algorithm to align the landmarks to the middle section of the high-resolution histologic slab.

2.2.8. Alignment of the MRI to the histological volume—Alignment of the MRI to the histology volume was achieved in 3 steps (Fig. 1F):

1. Approximately 10–20 matching landmarks (similar to those for the high-resolution histological volume composition previously mentioned) were manually labeled across multiple slices of the MRI and histology sections using the Montreal Neurological Institute's software Register (http://www.bic.mni.mcgill.ca/ServicesSoftwareVisualization/Register), reslicing with a 7–9 parameter rotation to achieve an initial overlap.
2. For a more precise alignment, landmarks were selected primarily within a slice. Both transformations were combined into a 9-parameter linear transformation. In 1 specimen (A4), this second step did not qualitatively enhance the alignment and was not performed.
3. Approximately 20 landmarks were manually selected in Fiji in each MRI slice matching each corresponding histologic section. Landmark Correspondences were again used to apply a nonlinear transformation using the moving least squares algorithm, achieving a very high quality alignment (bottom right, Fig. 2B).

For the control specimens that had been scanned with 7T MRI, we triple stained a single slice at the center of the slab, and this was approximately aligned with the histologic volume by manually reformatting the MRI for the best matching slice using OsiriX (www.osirix-viewer.com).

2.2.9. Segmentation of histological images—To determine the location of iron in AD, all separated histological stains were automatically segmented using Fiji. The entire histological slide was segmented. A histological exclusion mask was manually defined on each section to exclude the image edges by selecting the background using the magic wand function of Fiji. Additionally, regions of interest were drawn around the larger congested blood vessels and widened perivascular spaces characteristic of formalin embedded tissue, as well as of gross histology artifacts (i.e., tissue tears or gaps) (Fig. 2D, bottom left). The masks were dilated by 100–400 pixels to ensure adequate exclusion and applied to the successive stains within a single section.

The DAB-iron and phospho-tau-AT8 stains were Fourier bandpass filtered using Fiji (from 0 to 50 pixels at full resolution) to remove background heterogeneity and facilitate intensity-based segmentation of the entire microscopic slide (Fig. 2A, bottom left, and 2D, bottom left). The other stains, likely due to the subtractions incorporated in their computation, did not exhibit this inhomogeneity and did not require filtration. The individual stains were automatically segmented using Fiji’s Color-Threshold option (http://rsbweb.nih.gov/ij/docs/guide/146-28.html#toc-Subsection-28.2). (1) For automatic DAB-iron segmentation performed after bandpass filtering, we found that selecting a range of huesaturation-brightness (HSB) filtration values performed an adequate segmentation of all iron deposits using the following parameters: a hue including from 0 to 255, saturation including from 0 to 255, and brightness including from 0 to 150–210. The range of 150–210 represents a range in the upper brightness threshold across specimens; this upper limit on brightness was manually adjusted so that subjectively all of the dense DAB-iron spots were segmented avoiding faint background segmentation (red outline in Fig. 2B). This thresholding procedure ensured that lipofuscin granules (which are stained weakly brown) were not segmented as they are not representative of iron. (2) For CD163, red-green-blue segmentation isolated the blue staining with the following parameters: red including from 0 to 194–220 (also adjusted in a similar manner, red outline in Fig. 2B), green including from 0 to 220, and blue including from 0 to 255. (3) For Aβ, HSB filtration identified all the red amyloid deposits with the following parameters: a hue excluding 27 to 214–224 (thereby including 0–26 as well as 214/224–255), a saturation including from 28–56 to 255, and a brightness including from 0 to 255. (4) For phospho-tau after bandpass filtering, which stains a similar brown to DAB-iron, we used laboratory filtration with the following parameters: “L” including from 0 to 225–235, “a” including from 121 to 255, and “b” including from 0 to 255. In all cases, Fiji’s watershed filter (http://fiji.sc/Particle_Analysis) was applied to separate adjacent segmented structures. Finally, Fiji’s analyze particles option was used to segment each stain into separate foci, using a minimum size threshold of 25 pixels.

2.2.10. Segmentation of MRI—An MR mask was similarly created encompassing the image edges and the larger blood vessels (Fig. 2D, top row, left column). Blood vessels and perivascular spaces (which would appear identical, either containing clot or Fluorinert, both black on MRI) were identified as hypointense tubular structures. To preserve comparability across specimens, we masked out everything lateral to the stem of the parahippocampal gyrus by drawing a line between the inferior tip of the temporal horn of the lateral ventricle and the depth of the collateral sulcus (Fig. 6, top row, straight red lines at the left side of each image). Image filtration was used to emphasize the signal voids and remove background intensity: using Fiji, the image was resampled to 750 × 750 pixels in size, edge-filtered with a 5 × 5 kernel (−24 in the center, +1 at all other positions), and upsampled to histology resolution (Fig. 2D). Of note, the MR segmentation was not binary but was an intensity image that quantified the distribution of hypointensity.

2.2.11. Characterizing etiology of MR hypointensities—Because it was difficult to achieve an exact alignment between 2D serial histologic sections and 3D MRI and identify exact correspondences between individual signal voids and histology, we sought to compare the spatial distribution of signal voids on the MRI with the spatial distributions of the different stains across the specimens by creating a quantitative density map (Fig. 2D). First, the MR mask was applied to the coregistered MRI and histology stains. Then, for the histologic quantitative density map, a spatial distribution was computed by creating a histogram of bin size 300 pixels at histologic resolution using MATLAB's hist3 function (Mathworks, Natick, MA, USA). For coregistered serial slices of the iron, microglia, or Aβ stains, the quantitative density maps were averaged across pixels that were not within the slice-specific histological exclusion mask. For the MR quantitative density map, the MR segmentation was resampled to the size of the histological quantitative density map using MATLAB's imresize function. To account for partial volume artifact after resizing the MR mask, a pixel in each quantitative density map was conservatively masked out if 10% or more of the corresponding source pixels before resizing were masked out in the source MR mask. All quantitative density maps were then smoothed with a Gaussian filter of 7 pixels and width and a sigma of 1.25 pixels to accommodate minor errors in registration using the MATLAB functions fspecial and ndnanfilter. After logarithmic transformation of all quantitative density maps (discarding the rare pixels that had a quantitative density of 0 on any of the maps), a Pearson's correlation was performed pixelwise between each of the stains and the MRI segmentation (Fig. 6, top right corner of each histological quantitative density map). Additionally, a regression model was created in Stata (StataCorp LP) in which log MR quantitative density was the dependent variable to be explained, and log quantitative densities of iron, microglial, Aβ, and phospho-tau were independent variables. The model also included a constant term and the interaction of iron with microglia (a histological entity known as a siderophage (Grundke-Iqbal et al., 1990)) as well as iron with amyloid (because iron is known to colocalize with amyloid plaques (Lovell et al., 1998)). Specimen identification number was included as the cluster variable.

2.2.12. Quantification of etiology of iron—Because microscopic iron could have potential as a disease marker, it is important to know if the iron is part of an amyloid plaque pertaining to amyloid pathology, part of a microglial siderophage pertaining to inflammation, or unrelated. We could address this question by quantifying the degree of overlap between the DAB-iron stain and/or the microglial and/or amyloid stains. For each segmented DAB-iron deposit above an area threshold of 25 pixels (3.35 × 3.35 μm), we identified the most overlapping CD163 and amyloid segmented spots using a python script within Fiji (Fig. 2C). Then, we computed the extent of overlap with CD163 and amyloid, computed as the percentage of the number of overlapping pixels to the total area of the iron deposit. This overlap was thresholded at a minimum of 2 pixels and 2% of the area of the iron deposit for Table 2. The CD163 and amyloid percentage overlaps were compared with a paired *t* test (n = 4).

3. Results

3.1. Specimen MRI

Scanning of the medial temporal lobe at 100-μm isotropic resolution with 7T MRI demonstrated exquisite anatomic detail, clearly showing the microanatomy and lamination of the hippocampus similar to other efforts with specimen MRI (Figs. 1C, 4, 5) (Adler et al., 2014; Augustinack et al., 2014).

3.2. Alzheimer MR microscopy

Four of 5 medial temporal lobe AD specimens were at the level of the hippocampal body: these 4 demonstrated numerous very dark and tiny signal voids concentrated primarily in the subiculum, extending into the subjacent subcortical white matter (Figs. 4–6, Supplementary Movies 1–5). The signal voids sometimes coalesced into less discreet patches or streaks of hypointensity. One AD specimen (A2) was more anterior at the level of the hippocampal head and did not demonstrate these signal voids. Elsewhere in the hippocampus and entorhinal and/or parahippocampal regions, much less discrete hypointensities were present. The 5 normal control specimens scanned at 7T did not demonstrate these concentrated hippocampal signal voids (Fig. 9, Supplementary Movie 6), though 1 specimen (N3) demonstrated a very subtle neuropil defect along the undersurface of CA1 (Fig. 9, red box, Supplementary Movie 7). Throughout the remainder of the neocortex, no similar clusters of marked hypointensity were present (Fig. 4).

3.3. Alzheimer MR-histology correlation

To determine the etiology of the subicular-CA1 signal voids in the 4 hippocampal body AD specimens, we compared and performed a pixelwise correlation between the DAB-iron, CD 163, Aβ, and phospho-tau-AT8 quantitative density maps and the MRI. We will discuss each specimen separately (Figs. 6 and 7). A1 demonstrated signal voids primarily in the subiculum. This colocalized strongly with DAB-iron staining, and CD163 similarly was concentrated in this region. Amyloid was primarily localized to the collateral sulcus and adjacent parahippocampal gyrus and was not present in this region of the subiculum (Fig. 7). Although tau was also localized to the collateral sulcus and additionally concentrated in the superior CA fields, increased tau can be seen in the same region of the subiculum, primarily in the form of neuropil threads (Fig. 7). A3 shows hypointense foci also within the subiculum. Iron and CD163 were both concentrated in the same locations within the subiculum as the MRI. CD163 also showed staining more proximally in CA1 and along the undersurface of the parahippocampal gyrus. Amyloid demonstrated partial overlap with the low MR signal foci in the proximal subiculum (Fig. 7) as well as parahippocampal deposition. Tau was present throughout the subiculum in the form of both tangles and neuropil threads (Fig. 7), and tau was also present in CA1 as well as the collateral sulcus. A4 signal voids populate primarily the proximal subiculum and to a lesser extent CA1 both its deep portion and superficially along the hippocampal sulcus. This is highly correlated with iron and CD163. Amyloid is less concentrated in particular at the subiculum and more heavily concentrated along the more proximal CA1 and collateral sulcus. Tau was well correlated in the subiculum as well as CA1 in the form of tangles and threads, but like amyloid also demonstrated extensive deposition along the collateral sulcus. A5 demonstrated extensive hypointense foci concentrated in the subiculum and very highly correlated with iron. Microglia were similarly well correlated in the same region and extended further into CA1 and the parahippocampal gyrus. Amyloid was present in the same region of iron deposition but much more widely dispersed. Tau overlapped well with the MRI but was heavily concentrated more proximally in CA1 and along the collateral sulcus, with numerous tangles and neuropil threads present. Taken together, the strongest and most consistent positive correlation was found between the MRI and DAB-iron primarily in the subiculum (Fig. 6), an expected finding given the known sensitivity of high-field MRI to microscopic iron. CD163 had the next-most consistent correlation with the MRI. Phosphotau-AT8 was the next-most correlated followed by Aβ, which demonstrated an inconsistent correlation with the MRI across the specimens. Both the DAB-iron and CD163 tended to be most concentrated at the same subiculum location where MR hypointense foci were detected (Figs. 6 and 7), while amyloid and phospho-tau were not as uniformly concentrated primarily in these locations. A regression model explaining MR quantitative density by the histologic quantitative density maps identified that the only significant factor was the interaction of iron andmicroglia ($p = 0.025$). Other effects were not significant: iron ($p = 0.068$), microglia ($p = 0.137$), Aβ ($p = 0.184$), phospho-tau ($p = 0.335$), and the Aβ-iron interaction ($p = 0.291$). Taken together, these results suggest that the hypointense foci on MRI arise from iron-containing microglia.

None of the control specimens demonstrated a similar accumulation of iron-containing microglia within the subiculum. N1 and N2 were both negative with some perivascular resting microglia (Fig. 9). N3 showed an aggregate of microglia in the subpial segment of CA1, containing much less iron than in the AD specimens, in the absence of Aβ and tau (Fig. 9, red and black boxes). Inspection of the adjacent hematoxylin-and eosin-stained sections showed this to be a region of microinfarction with expected associated gliosis and microglial activation (Fig.10), matching the defect on MRI. N4 and N5 showed only mild senile changes in the form of trace amyloid along the collateral sulcus, without any correlate on MRI (Fig. 9). Three additional control specimens, from older individuals with histological staining only, also did not show the same finding of iron-containing microglia within the subiculum (Fig. 11). N6 showed faint staining with the iron preparation without dense iron deposits, microglia activation, amyloid, or tau accumulation. N7 showed autolysis and was otherwise negative. N8 demonstrated a few amyloid plaques, tangles, and neuropil threads, again representing mild senile changes.

3.4. Histologic localization of microscopic iron in AD

With coregistered DAB-iron, CD 163, and Aβ segmentations, we sought to determine the localization of iron with respect to microglia and Aβ by examining the pixel-based overlap of individual iron deposits (Fig. 2C). In the 4 AD specimens, there was greater overlap of iron with microglia compared with iron with Aβ (Table 2, $p = 0.047$). Some iron was extracellular in location, overlapping with neither microglia nor amyloid, reflecting parenchymal hemosiderin. A direct comparison with phospho-tau was not possible because this stain was on interleaved slices. Fig. 8 demonstrates typical examples of iron-containing activated microglia, or siderophages, from each specimen, again from the subiculum.

4. Discussion

Using ultra-high field 7T ex vivo MRI of AD, we identified focal hypointensities located in the hippocampus in AD, specifically primarily within the subiculum, a novel imaging finding that could be specific for AD. Coregistration of the MRI with the histology suggested that these foci represent iron deposits that may largely be within microglia, also known as siderophages. This finding was neuropathologically present in concentrated form in most of the AD cases, and not within the control specimens. Although one of the control specimens showed microglia in the hippocampus, this was in a region of microinfarction associated with a subtle neuropil defect on MRI, showed substantially less microglial iron in comparison to the AD pathology, and demonstrated an absence of Aβ and tau pathology, suggesting an unrelated, incidental microinfarct. Given the subiculum is the key location where entorhinal perforant and alvear pathway neurons cross en route to the hippocampus (Witter and Amaral, 1991), the microglial activity identified here could possibly represent entorhinal neurodegeneration, known to be significant at an early stage of AD (Gómez-Isla et al., 1996). This location may also correlate with the path of trans-synaptic spread of tau identified in murine models (de Calignon et al., 2012), and in our study tau was present in this same location in subiculum. Our results should motivate further research on the role of iron and microglia in AD, complementary and synergistic with amyloid and tau. Although there is an established progression of Aβ plaques and neurofibrillary tangles (Braak and Braak, 1991; Mirra et al., 1991; Thal et al., 2000), very little is known about the progression of iron and microglia across the stages of AD throughout the brain. Similarly, there is the potential for iron to become a biomarker for the inflammatory component of AD using in vivo high-field MRI, and this could form the basis of developing and monitoring antiinflammatory interventions.

A growing body of ex vivo work is investigating the role of both iron (Connor et al., 1992; Deibel et al., 1996; Grundke-Iqbal et al., 1990; Lovell et al., 1998; Quintana et al., 2006) and microglia (Colton et al., 2014; Gallagher et al., 2012; Gandy and Heppner, 2013; Griciuc et al., 2013; McGeer and McGeer, 2013; Zhang et al., 2013) in AD. Although past attempts at visualizing AD pathology with MRI initially focused on amyloid (Meadowcroft et al., 2009), recent direct studies of iron in AD combined ex vivo MR imaging with synchrotron microfocus X-ray fluorescence microscopy to show a correlation of iron with the MR relaxation parameter R2* (Antharam et al., 2012). In AD, there was a wider histogram of R2* distributions in the hippocampus, the right tail of which may correspond with increased iron deposition. Our study bridges the neuropathologic literature on iron and microglia with the field of MR microscopy to link MRI hypointensities with iron deposits inside of microglia.

Neuropathological-specific in vivo imaging of AD has focused on Aβ, with fluorinated positron emission tomography (PET) variants of Pittsburgh compound B advancing as the likely standard for identifying plaques. However, the more important toxic amyloid oligomers are a heterogeneous entity (Lesne, 2013) not visualized by these PET tracers (Bao et al., 2012; Niedowicz et al., 2012). Tau-based agents have shown rapid progress, but these tracers have thus far predominantly been positive late in the disease (Chien et al., 2013). Several PET studies have evaluated the distribution of microglia in AD by targeting the translocator protein 18kD (Venneti et al., 2013); the most common of these agents is named ^{11}C-PK11195. A direct comparison of ^{11}C-PIB and ^{11}C-PK11195 has shown similar patterns of uptake for both tracers, though ^{11}CPK11195 showed overall less uptake and relative sparing of the hippocampi (Edison et al., 2008). However, another study employing the same 2 tracers showed left hippocampal PK11195 uptake inversely correlated with the Mini-Mental Status Examination (Yokokura et al., 2011). Overall, the PET literature suggests an association between microglia and amyloid, but localization to the medial temporal lobe has not been confirmed. Because of high-field MRI’s unique sensitivity to iron, there could be a role for in vivo MR detection of microglia associated with AD. In spite of the extremely small size of these lesions, direct visualization with ultra-high field in vivo MR may be possible if the challenges of high-resolution and patient motion can be addressed.

A combined analysis of MRI and histology inherently involves many challenges that should be taken into account when considering these results. Our alignment procedure addressed the difficult problem due to nonlinear distortions associated with histological sectioning and processing. Other approaches could also be effective and may involve less operator dependence (Adler et al., 2014; Axer et al., 2011). Our study did not employ the alternatively used CD68 immunostain for microglia because the use of anti-CD163 exhibits significantly lower background staining, permitting our bright-field subtraction and segmentation procedure. Direct inspection confirmed that the iron-containing microglia visualized were activated and not in a perivascular resting conformation (Fig. 8). We chose to use bright-field microscopy rather than immunofluorescence to avoid background staining from autofluorescent lipofuscin granules and permit quantitative density mapping. Our segmentation employed thresholding to ensure that we avoided lipofuscin granules (which can appear brown on bright-field microscopy of numerous stains in AD) and segmented only the stain of interest. The direct overlap between iron and microglia was not uniform across specimens, but always substantially greater for microglia than for amyloid. The incomplete overlap may be partially explained by cases where the CD163 stain primarily circumscribes and only minimally overlaps with iron, escaping detection by overlap quantification. Regardless, iron deposition was not always associated with microglia, and sometimes appeared extracellular in the form of hemosiderin. Although the microglia observed in this study were not consistently colocalized with amyloid, we are not measuring soluble amyloid, and in vitro work has shown that the overlap between amyloid and iron can be incomplete (Everett et al., 2014b). An additional factor in our data set is the advanced pathological stage of AD: tau pathology is extremely concentrated in the entorhinal region in late AD, and this may obscure correlations with subicular microglial pathology. Interestingly, 1 of our AD specimens did not show these MR hypointense foci at the subiculum, though this specimen was located more anteriorly at the hippocampal head, possibly before perforant pathway fibers become more concentrated. Nevertheless, it is possible that iron-microglial concentration at the subiculum is not a universal phenomenon in AD, or is variable across time as the disease progresses. Future work involving a larger sample size composed of different stages of AD and mild-cognitive impairment with an age-matched control population could clarify these issues. All our specimens were formalin fixed, and future studies can explore the role fixation may play in altering iron-content by examining unfixed AD hippocampal specimens (Antharam et al., 2012).

This early work suggests that activated iron-containing microglia may be present in the hippocampus in AD and visualized by ex vivo MRI. Given the specimens in our study were all late-stage AD, future work will characterize this finding ex vivo across the spectrum of AD and mild-cognitive impairment. Additionally, the pursuit of in vivo visualization with 7.0 T MRI may prove fruitful. Given the incomplete models of amyloid and tau, iron-associated inflammation could be considered a significant contributor to AD, ripe for further investigation.

Supplementary Material

Refer to Web version on PubMed Central for supplementary material.

Acknowledgments

The authors thank Dr. Karl Zilles and Dr. Nicola Palomero-Gallagher for their detailed assistance in segmenting the prosubiculum, Dr. Edward Plowey and Dr. Michelle James for their comments on this manuscript, Dr. Jarrett Rosenberg for his advice on statistical analyses, Jason Parnes for his assistance developing the slide scanning procedure, and Dr. Scott Atlas for his comments on MRI-histology interpretation. Dr. Zeineh received an RSNA Research Fellow Award that funded a portion of this research.

Dr. Michael Zeineh and Dr. Brian Rutt both receive research funding from General Electric Healthcare.

References

Adler DH, Pluta J, Kadivar S, Craige C, Gee JC, Avants BB, Yushkevich PA. Histology-derived volumetric annotation of the human hippocampal subfields in postmortem MRI. Neuroimage. 2014; 84:505–523. [PubMed: 24036353]

Antharam V, Collingwood JF, Bullivant JP, Davidson MR, Chandra S, Mikhaylova A, Finnegan ME, Batich C, Forder JR, Dobson J. High field magnetic resonance microscopy of the human hippocampus in Alzheimer's disease: quantitative imaging and correlation with iron. Neuroimage. 2012; 59:1249–1260. [PubMed: 21867761]

Arnold SE, Louneva N, Cao K, Wang LS, Han LY, Wolk DA, Negash S, Leurgans SE, Schneider JA, Buchman AS, Wilson RS, Bennett DA. Cellular, synaptic, and biochemical features of resilient cognition in Alzheimer's disease. Neurobiol. Aging. 2013; 34:157–168. [PubMed: 22554416]

Augustinack JC, Magnain C, Reuter M, van der Kouwe AJ, Boas D, Fischl B. MRI parcellation of ex vivo medial temporal lobe. Neuroimage. 2014; 93(Pt 2):252–259. [PubMed: 23702414]

Axer M, Amunts K, Grässel D, Palm C, Dammers J, Axer H, Pietrzyk U, Zilles K. A novel approach to the human connectome: ultra-high resolution mapping of fiber tracts in the brain. Neuroimage. 2011; 54:1091–1101. [PubMed: 20832489]

Bao F, Wicklund L, Lacor PN, Klein WL, Nordberg A, Marutle A. Different beta-amyloid oligomer assemblies in Alzheimer brains correlate with age of disease onset and impaired cholinergic activity. Neurobiol. Aging. 2012; 33:825.e1–825.e13. [PubMed: 21683475]

Benveniste H, Einstein G, Kim KR, Hulette C, Johnson GA. Detection of neuritic plaques in Alzheimer's disease by magnetic resonance microscopy. Proc. Natl. Acad. Sci. U. S. A. 1999; 96:14079–14084. [PubMed: 10570201]

Braak H, Braak E. Neuropathological stageing of Alzheimer-related changes. Acta Neuropathol. 1991; 82:239–259. [PubMed: 1759558]

Chien DT, Bahri S, Szardenings AK, Walsh JC, Mu F, Su MY, Shankle WR, Elizarov A, Kolb HC. Early clinical PET imaging results with the novel PHF-tau radioligand [F-18]-T807. J. Alzheimers Dis. 2013; 34:457–468. [PubMed: 23234879]

Collingwood JF, Chong RK, Kasama T, Cervera-Gontard L, Dunin-Borkowski RE, Perry G, Posfai M, Siedlak SL, Simpson ET, Smith MA, Dobson J. Three-dimensional tomographic imaging and characterization of iron compounds within Alzheimer's plaque core material. J. Alzheimers Dis. 2008; 14:235–245. [PubMed: 18560134]

Colton CA, Wilson JG, Everhart A, Wilcock DM, Puolivali J, Heikkinen T, Oksman J, Jaaskelainen O, Lehtimaki K, Laitinen T, Vartiainen N, Vitek MP. mNos2 deletion and human NOS2 replacement in Alzheimer disease models. J. Neuropathol. Exp. Neurol. 2014; 73:752–769. [PubMed: 25003233]

Connor JR, Menzies SL, St Martin SM, Mufson EJ. A histochemical study of iron, transferrin, and ferritin in Alzheimer's diseased brains. J. Neurosci. Res. 1992; 31:75–83. [PubMed: 1613823]

Davis DG, Schmitt FA, Wekstein DR, Markesbery WR. Alzheimer neuropathologic alterations in aged cognitively normal subjects. J. Neuropathol. Exp. Neurol. 1999; 58:376–388. [PubMed: 10218633]

de Calignon A, Polydoro M, Suarez-Calvet M, William C, Adamowicz DH, Kopeikina KJ, Pitstick R, Sahara N, Ashe KH, Carlson GA, Spires-Jones TL, Hyman BT. Propagation of tau pathology in a model of early Alzheimer's disease. Neuron. 2012; 73:685–697. [PubMed: 22365544]

Deibel MA, Ehmann WD, Markesbery WR. Copper, iron, and zinc imbalances in severely degenerated brain regions in Alzheimer's disease: possible relation to oxidative stress. J. Neurol. Sci. 1996; 143:137–142. [PubMed: 8981312]

Dhenain M, Privat N, Duyckaerts C, Jacobs RE. Senile plaques do not induce susceptibility effects in T2*-weighted MR microscopic images. NMR Biomed. 2002; 15:197–203. [PubMed: 11968135]

Ding SL. Comparative anatomy of the prosubiculum, subiculum, presubiculum, postsubiculum, and parasubiculum in human, monkey, and rodent. J. Comp. Neurol. 2013; 521:4145–4162. [PubMed: 23839777]

Edison P, Archer HA, Gerhard A, Hinz R, Pavese N, Turkheimer FE, Hammers A, Tai YF, Fox N, Kennedy A, Rossor M, Brooks DJ. Microglia, amyloid, and cognition in Alzheimer's disease: an [11C](R)PK11195-PET and [11C]PIB-PET study. Neurobiol. Dis. 2008; 32:412–419. [PubMed: 18786637]

Everett J, Cespedes E, Shelford LR, Exley C, Collingwood JF, Dobson J, van der Laan G, Jenkins CA, Arenholz E, Telling ND. Evidence of redox-active iron formation following aggregation of ferrihydrite and the Alzheimer's disease peptide beta-amyloid. Inorg. Chem. 2014a; 53:2803–2809. [PubMed: 24559299]

Everett J, Cespedes E, Shelford LR, Exley C, Collingwood JF, Dobson J, van der Laan G, Jenkins CA, Arenholz E, Telling ND. Ferrous iron formation following the co-aggregation of ferric iron and the Alzheimer's disease peptide beta-amyloid (1–42). J. R. Soc. Interface. 2014b; 11:20140165. [PubMed: 24671940]

Gallagher JJ, Finnegan ME, Grehan B, Dobson J, Collingwood JF, Lynch MA. Modest amyloid deposition is associated with iron dysregulation, microglial activation, and oxidative stress. J. Alzheimers Dis. 2012; 28:147–161. [PubMed: 21971404]

Gandy S, Heppner FL. Microglia as dynamic and essential components of the amyloid hypothesis. Neuron. 2013; 78:575–577. [PubMed: 23719156]

Goedert M, Jakes R. Mutations causing neurodegenerative tauopathies. Biochim. Biophys. Acta. 2005; 1739:240–250. [PubMed: 15615642]

Gómez-Isla T, Price JL, McKeel DW Jr, Morris JC, Growdon JH, Hyman BT. Profound loss of layer II entorhinal cortex neurons occurs in very mild Alzheimer's disease. J. Neurosci. 1996; 16:4491–4500. [PubMed: 8699259]

Griciuc A, Serrano-Pozo A, Parrado AR, Lesinski AN, Asselin CN, Mullin K, Hooli B, Choi SH, Hyman BT, Tanzi RE. Alzheimer's disease risk gene CD33 inhibits microglial uptake of amyloid beta. Neuron. 2013; 78:631–643. [PubMed: 23623698]

Grundke-Iqbal I, Fleming J, Tung YC, Lassmann H, Iqbal K, Joshi JG. Ferritin is a component of the neuritic (senile) plaque in Alzheimer dementia. Acta Neuropathol. 1990; 81:105–110. [PubMed: 2082650]

Lesne SE. Breaking the code of amyloid-beta oligomers. Int. J. Cell Biol. 2013; 2013:950783. [PubMed: 24072999]

Lovell MA, Robertson JD, Teesdale WJ, Campbell JL, Markesbery WR. Copper, iron and zinc in Alzheimer's disease senile plaques. J. Neurol. Sci. 1998; 158:47–52. [PubMed: 9667777]

McGeer PL, McGeer EG. The amyloid cascade-inflammatory hypothesis of Alzheimer disease: implications for therapy. Acta Neuropathol. 2013; 126:479–497. [PubMed: 24052108]

Meadowcroft MD, Connor JR, Smith MB, Yang QX. MRI and histological analysis of beta-amyloid plaques in both human Alzheimer's disease and APP/PS1 transgenic mice. J. Magn. Reson. Imaging. 2009; 29:997–1007. [PubMed: 19388095]

Mirra SS, Heyman A, McKeel D, Sumi SM, Crain BJ, Brownlee LM, Vogel FS, Hughes JP, van Belle G, Berg L. The Consortium to Establish a Registry for Alzheimer's Disease (CERAD). Part II. Standardization of the neuropathologic assessment of Alzheimer's disease. Neurology. 1991; 41:479–486. [PubMed: 2011243]

Niedowicz DM, Beckett TL, Matveev S, Weidner AM, Baig I, Kryscio RJ, Mendiondo MS, LeVine H 3rd, Keller JN, Murphy MP. Pittsburgh compound B and the postmortem diagnosis of Alzheimer disease. Ann. Neurol. 2012; 72:564–570. [PubMed: 23109151]

Pankhurst Q, Hautot D, Khan N, Dobson J. Increased levels of magnetic iron compounds in Alzheimer's disease. J. Alzheimers Dis. 2008; 13:49–52. [PubMed: 18334756]

Preibisch S, Saalfeld S, Tomancak P. Globally optimal stitching of tiled 3D microscopic image acquisitions. Bioinformatics. 2009; 25:1463–1465. [PubMed: 19346324]

Quintana C, Bellefqih S, Laval JY, Guerquin-Kern JL, Wu TD, Avila J, Ferrer I, Arranz R, Patiño C. Study of the localization of iron, ferritin, and hemosiderin in Alzheimer's disease hippocampus by analytical microscopy at the subcellular level. J. Struct. Biol. 2006; 153:42–54. [PubMed: 16364657]

Quintana C, Cowley JM, Marhic C. Electron nanodiffraction and high-resolution electron microscopy studies of the structure and composition of physiological and pathological ferritin. J. Struct. Biol. 2004; 147:166–178. [PubMed: 15193645]

Rosene, D.; Van Hoesen, G. The hippocampal formation of the primate brain. A review of some comparative aspects of cytoarchitecture and connections. In: Jones, E.; Peters, A., editors. Cerebral Cortex Further aspects of cortical function, including hippocampus. Vol. 6. New York: Plenum; 1987. p. 345-456.

Schindelin J, Arganda-Carreras I, Frise E, Kaynig V, Longair M, Pietzsch T, Preibisch S, Rueden C, Saalfeld S, Schmid B, Tinevez JY, White DJ, Hartenstein V, Eliceiri K, Tomancak P, Cardona A. Fiji: an open-source platform for biological-image analysis. Nat. Methods. 2012; 9:676–682. [PubMed: 22743772]

Selkoe DJ. Biochemistry and Molecular Biology of Amyloid b-Protein and the Mechanism of Alzheimer's Disease. Handb Clin Neurol. 2008; 89:245–260. [PubMed: 18631749]

Sheng JG, Mrak RE, Griffin WS. Microglial interleukin-1 alpha expression in brain regions in Alzheimer's disease: correlation with neuritic plaque distribution. Neuropathol. Appl. Neurobiol. 1995; 21:290–301. [PubMed: 7494597]

Smith MA, Harris PL, Sayre LM, Perry G. Iron accumulation in Alzheimer disease is a source of redox-generated free radicals. Proc. Natl. Acad. Sci. U. S. A. 1997; 94:9866–9868. [PubMed: 9275217]

Spires-Jones TL, Hyman BT. The intersection of amyloid beta and tau at synapses in Alzheimer's disease. Neuron. 2014; 82:756–771. [PubMed: 24853936]

Tanzi RE. The genetics of Alzheimer disease. Cold Spring Harb. Perspect. Med. 2012; 2:1–10.

Terry RD, Masliah E, Salmon DP, Butters N, DeTeresa R, Hill R, Hansen LA, Katzman R. Physical basis of cognitive alterations in Alzheimer's disease: synapse loss is the major correlate of cognitive impairment. Ann. Neurol. 1991; 30:572–580. [PubMed: 1789684]

Thal DR, Rüb U, Schultz C, Sassin I, Ghebremedhin E, Del Tredici K, Braak E, Braak H. Sequence of Abeta-protein deposition in the human medial temporal lobe. J. Neuropathol. Exp. Neurol. 2000; 59:733–748. [PubMed: 10952063]

Tomic JL, Pensalfini A, Head E, Glabe CG. Soluble fibrillar oligomer levels are elevated in Alzheimer's disease brain and correlate with cognitive dysfunction. Neurobiol. Dis. 2009; 35:352–358. [PubMed: 19523517]

Venneti S, Lopresti BJ, Wiley CA. Molecular imaging of microglia/macrophages in the brain. Glia. 2013; 61:10–23. [PubMed: 22615180]

Witter MP, Amaral DG. Entorhinal cortex of the monkey: V. Projections to the dentate gyrus, hippocampus, and subicular complex. J. Comp. Neurol. 1991; 307:437–459. [PubMed: 1713237]

Yokokura M, Mori N, Yagi S, Yoshikawa E, Kikuchi M, Yoshihara Y, Wakuda T, Sugihara G, Takebayashi K, Suda S, Iwata Y, Ueki T, Tsuchiya KJ, Suzuki K, Nakamura K, Ouchi Y. In vivo changes in microglial activation and amyloid deposits in brain regions with hypometabolism in Alzheimer's disease. Eur. J. Nucl. Med. Mol. Imaging. 2011; 38:343–351. [PubMed: 20844871]

Zhang B, Gaiteri C, Bodea LG, Wang Z, McElwee J, Podtelezhnikov AA, Zhang C, Xie T, Tran L, Dobrin R, Fluder E, Clurman B, Melquist S, Narayanan M, Suver C, Shah H, Mahajan M, Gillis T, Mysore J, MacDonald ME, Lamb JR, Bennett DA, Molony C, Stone DJ, Gudnason V, Myers AJ, Schadt EE, Neumann H, Zhu J, Emilsson V. Integrated systems approach identifies genetic nodes and networks in late-onset Alzheimer's disease. Cell. 2013; 153:707–720. [PubMed: 23622250]

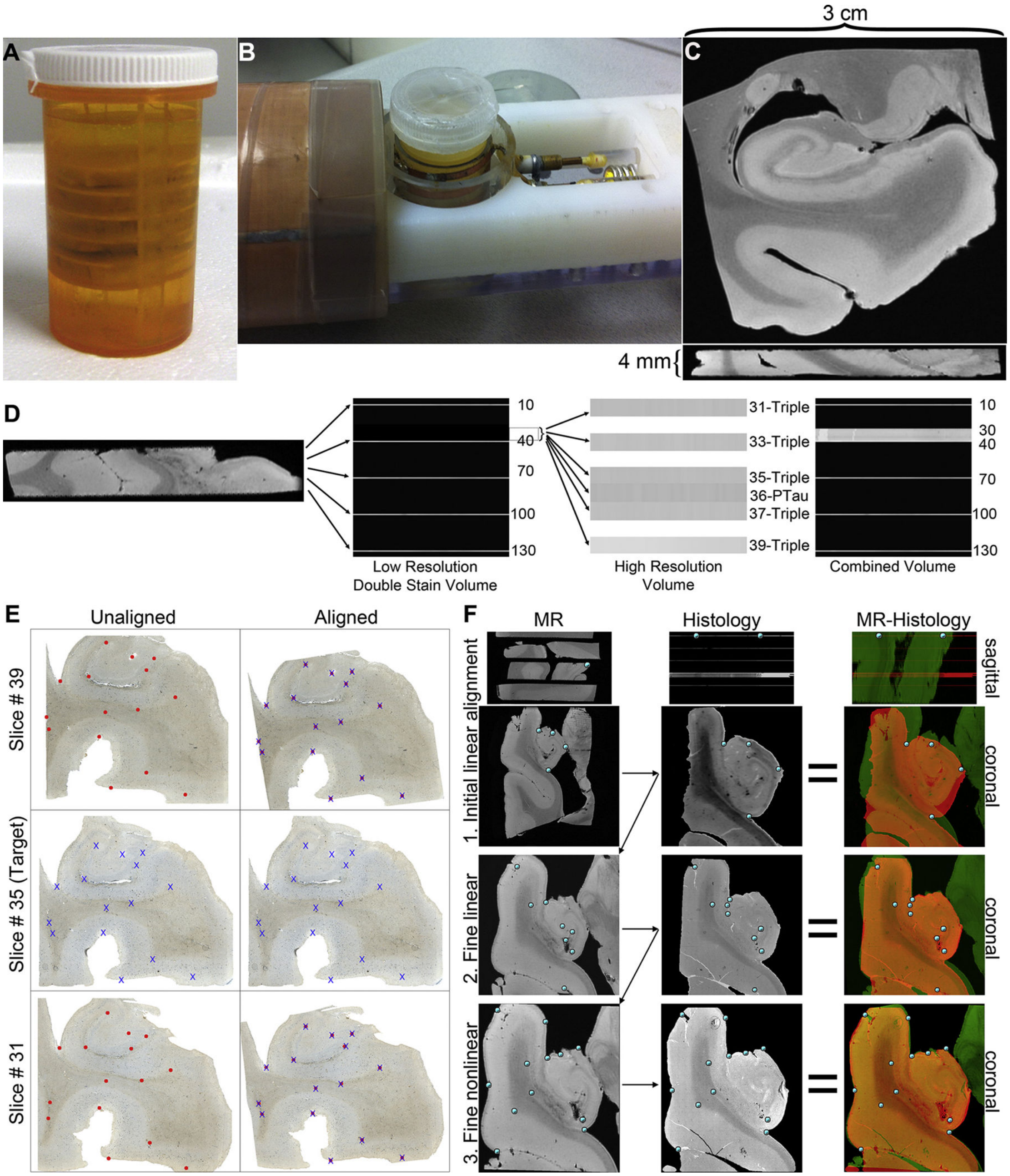

Fig. 1.

MR acquisition, histologic sectioning, and alignment procedure. (A–C) Specimen container, solenoid coil, and example coronal (top) and axial (bottom) MR images. (D) Histology sectioning protocol. The histology volume consists of 3,3’-diaminobenzidine (DAB)-CD163 double stains, comprised of the widely spaced low-resolution sections combined with the densely sampled high-resolution sections. Numbers indicate the histological section number. Triple = successive triple staining, P-tau = phospho-tau-AT8 single staining. (E) Alignment of serial histological sections. Fiducial points (vessels, perivascular spaces, tissue edges, and the gray-white junction) were chosen across serial double-stained (DAB-CD163) sections to match the underlying anatomy (red circle = source fiducials on the left, transformed fiducials on the right; blue X's = target, in the same position on all sections). (F) Three stages of alignment of MRI to histology. The top row contains sagittal and coronal reformations of the MR and histology volumes before (left and middle panel) and after (right panel, MR is green and histology red) a linear alignment over the whole 3-D volume as a first approximation. The middle row demonstrates a more exact linear alignment, tailored to landmarks within a slice. The bottom row depicts a nonlinear warping transformation for the most exact match. Abbreviations: MR, magnetic resonance. (For interpretation of the references to color in this figure legend, the reader is referred to the Web version of this article.)

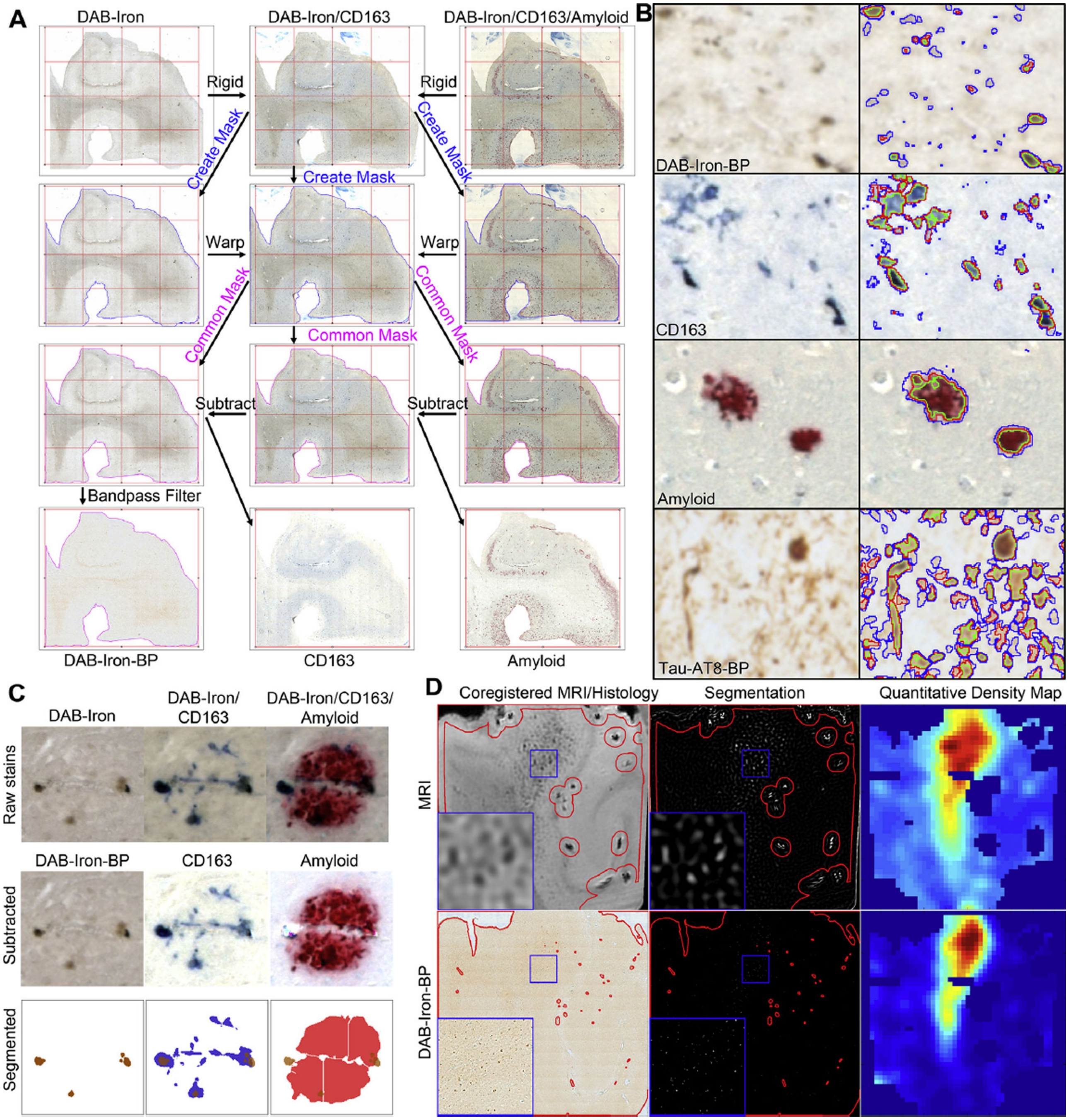

Fig. 2.

Successive histologic stain separation, thresholding, segmentation, and quantitative density mapping. (A) Alignment and subtraction procedure from specimen A4. Slides were scanned after successive stains. Initial rigid-body alignment (1st row) was followed by nonlinear warping, using individual tissue masks (2nd row, blue outline). After applying a common mask (purple), digital subtraction in units of optical density delivered the individual stains. Single stains (DAB-iron and phospho-tau-AT8) were bandpass filtered to improve homogeneity for segmentation. Because of the embedded subtractions, filtration was unnecessary for the CD163 and Aβ stains. (B) Segmentation of DAB-iron, CD163, amyloid, and tau-AT8 from specimen A4. In each example, blue indicates too liberal a segmentation threshold with too much inclusion of nonspecific background staining, green is too strict a segmentation threshold missing the iron, microglia, amyloid, or tau (in the form of neuropil threads, neurofibrillary tangles, and neuritic plaques), and red achieves a balance between the blue and green thresholds. Depicted thresholds in order of increasing sensitivity are as follows: DAB-iron hue-saturation-brightness (HSB) brightness of 180, 200, and 220 (green, red, and blue); CD163 upper red threshold 164, 194, and 224, amyloid HSB saturation lower threshold of 86, 56, and 26, and tau-AT8 lab filtration “L” channel upper threshold of 224, 229, and 234. (C) Segmenting coregistered stains from specimen A5: raw stains are aligned successive stains before any subtraction and/or filtration, subtracted are filtered and/or separated stains, and segmented depicts DAB-iron (brown), CD163 (blue), Aβ (red), with the DAB-iron segmentation overlaid on the CD163 and Aβ segmentations. (D) Quantitative density mapping from specimen A5. After masking blood vessels and perivascular spaces (curvilinear structures on serial images), artifacts, and tissue edges (red lines in left column), we segmented the MR and histology stains (middle column), and histogram binned and smoothed (right column) after combining masks across serial sections. The blue box is approximately 1.5 mm in width, zoomed at the bottom left corner. All images were windowed to emphasize the pathological item of interest. Abbreviations: DAB, 3,3’-diaminobenzidine; MRI, magnetic resonance imaging. (For interpretation of the references to color in this figure legend, the reader is referred to the Web version of this article.)

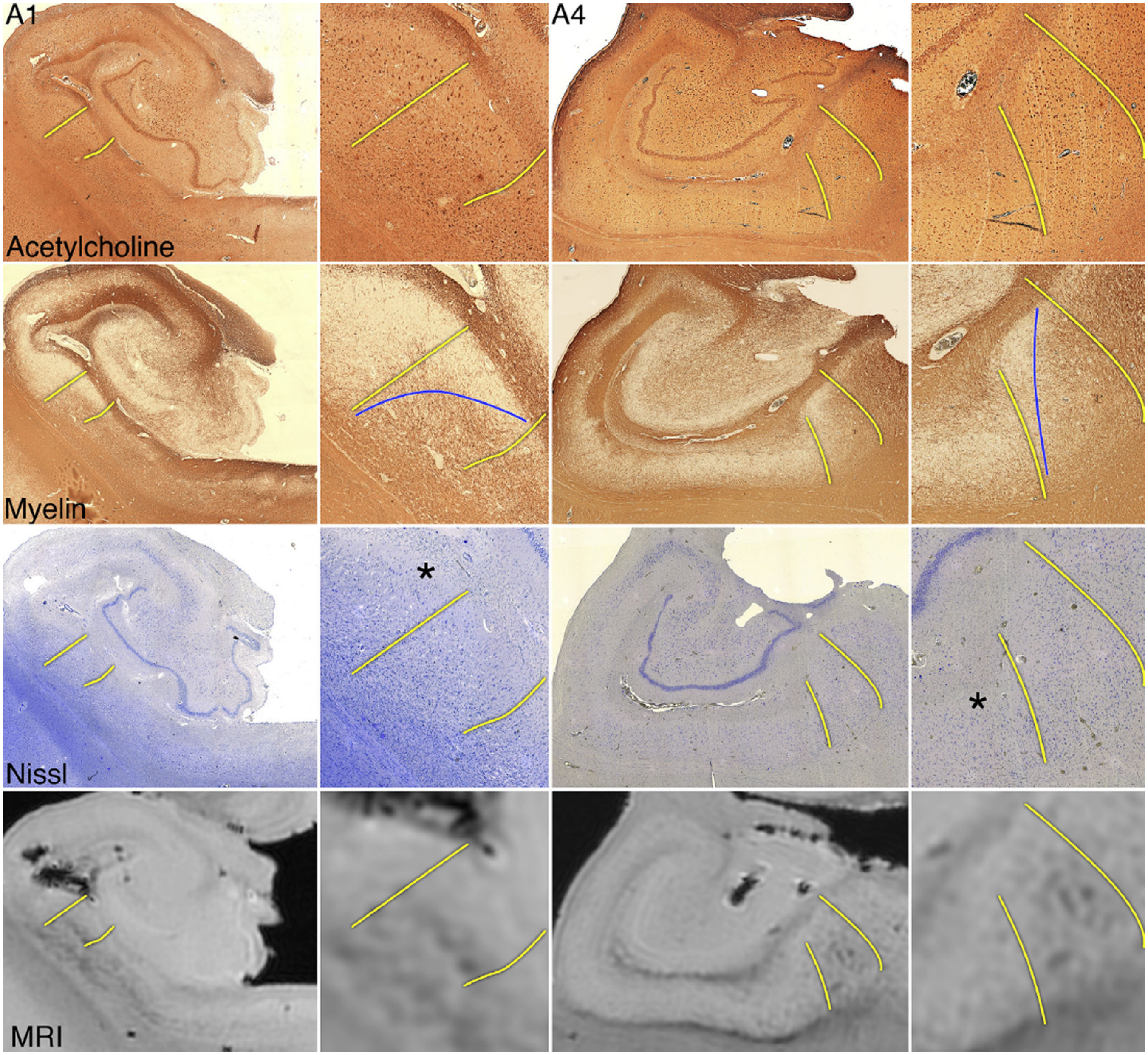

Fig. 3.

Histologic staining procedure to determine the junction of CA1 and the subiculum. The prosubiculum, outlined in yellow, is the most lateral and proximal field of the subiculum. The prosubiculum can be identified by the more intense acetylcholine staining, band-like increase in myelin staining the extends from the deep to superficial pyramidal cell layer (highlighted in blue), and disappearance of the cell-sparse radiatum layer that is present in CA1 (asterisk (*) on Nissl stain). The location of the prosubiculum can vary dramatically across specimens with respect to conventional imaging-based landmarks. For example, the medial aspect of the hippocampal body is a commonly used landmark for the junction between CA1 and the subiculum, but this would be quite inaccurate for case A1.

Abbreviation: MRI, magnetic resonance imaging. (For interpretation of the references to color in this figure legend, the reader is referred to the Web version of this article.)

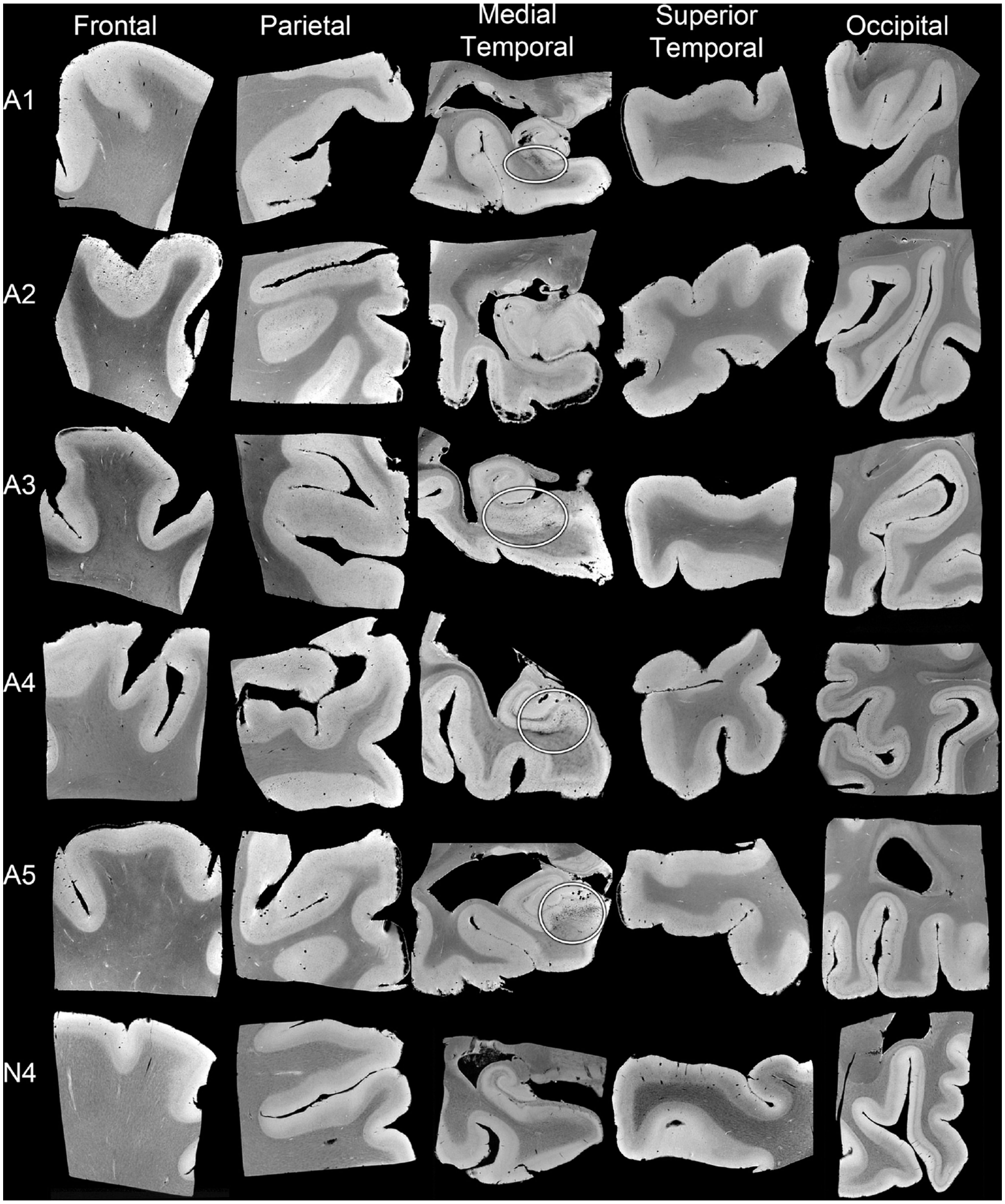

Fig. 4.

Whole-brain high resolution gradient echo specimen magnetic resonance imaging. A1–A5 represents the 5 Alzheimer disease (AD) specimens. N4 is a normal control. The AD specimens, except for specimen A2, demonstrate numerous signal voids in the region of the subiculum. None of the control specimens demonstrate similar signal voids. The sections were rotated, zoomed, and windowed to have a similar contrast. The line of Gennari is visible as the dark line running tangentially with the pial surface at the mid to deep portion of the cortex in most of the occipital lobe specimens. Most of the other large dark spots in the cortex and white matter across all specimens and lobes represent blood vessels or perivascular spaces.

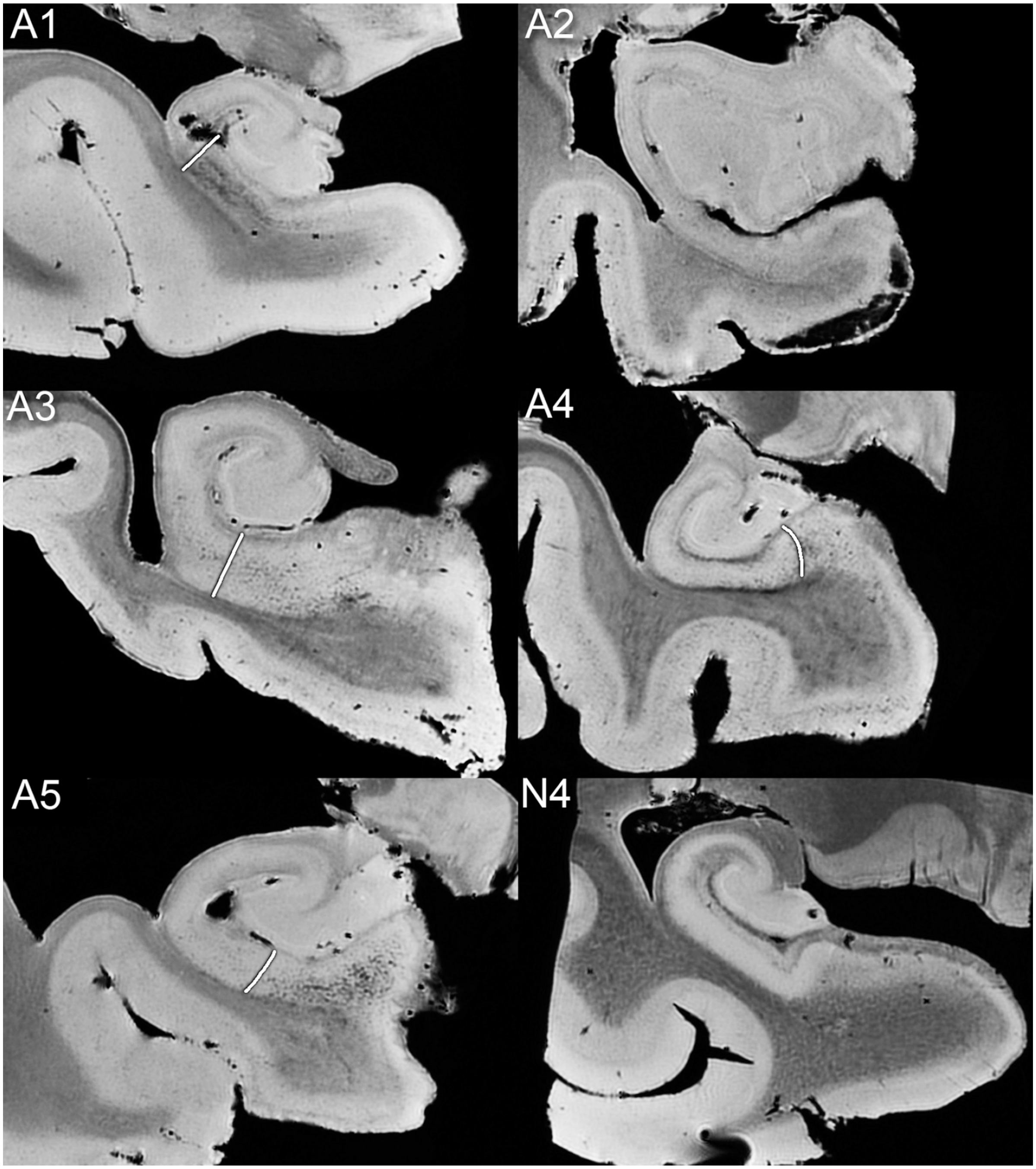

Fig. 5.

Medial temporal lobe specimen gradient echo magnetic resonance images. A1–A5 represents the 5 Alzheimer disease (AD) specimens. N4 is a normal control. The white line demarcates the location of the junction between CA1 and the subiculum (the proximal prosubiculum boundary). The AD specimens, except for specimen A2, demonstrate numerous signal voids primarily centered in the subiculum, extending toward and sometimes into the subjacent white matter. None of the control specimens demonstrate similar signal voids. Images were windowed to display similar contrast between gray and white matter.

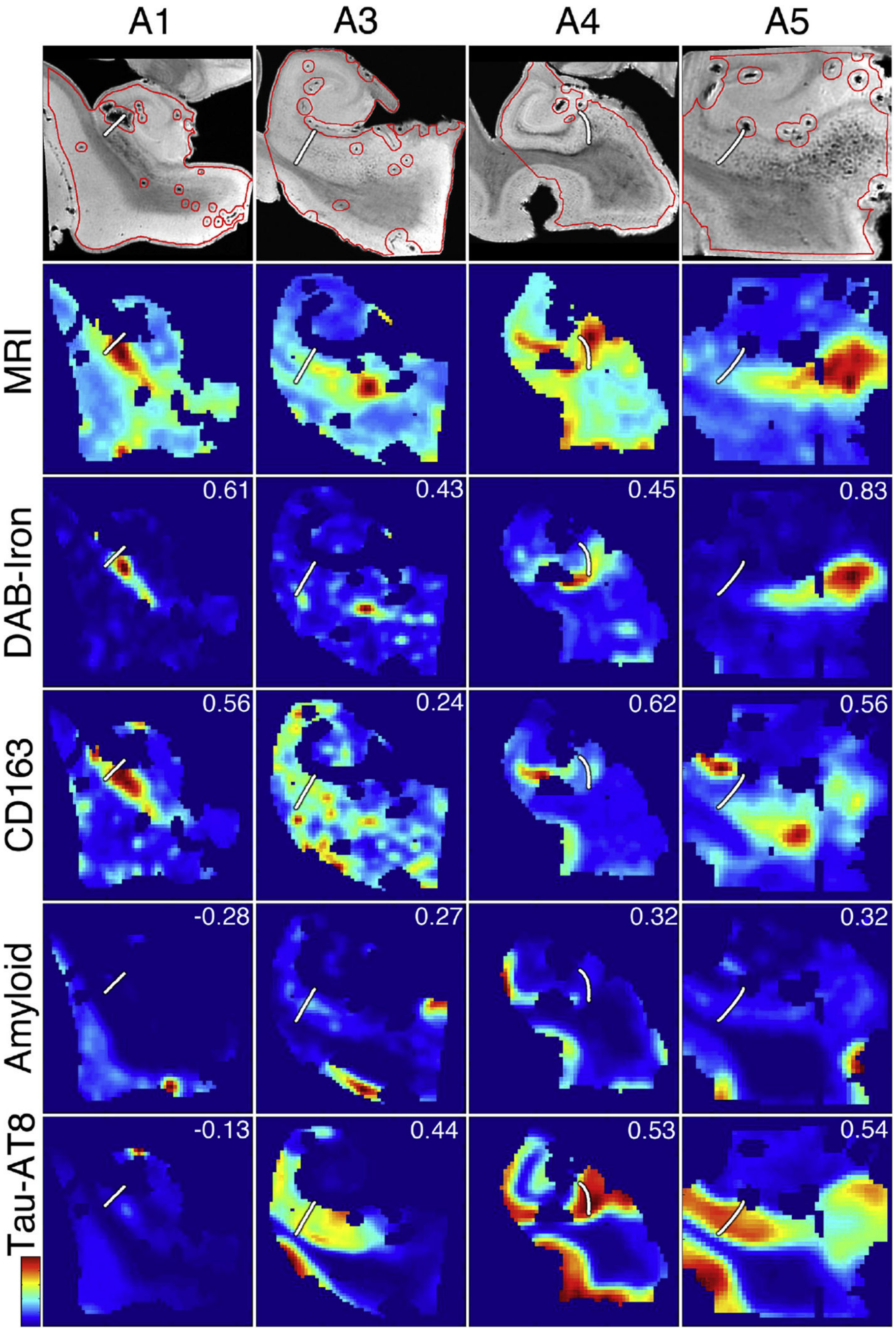

Fig. 6.

Top row: representative MRI from each specimen. MRI: quantitative density of MR hypointense foci. DAB-iron, CD163, amyloid beta (Aβ), and phospho-tau-AT8 represent the respective quantitative density maps of these stains averaged across all coregistered slices within specimen. The color scale and bar are in arbitrary units. The white line/curve indicates the border between field CA1 and the prosubiculum (the most proximal cell field of the subiculum). The number at the top right corner is the Pearson's correlation between the logarithm of quantitative density in the given stain and logarithm of quantitative density of the MRI. Signal voids primarily in the proximal subiculum appear red on the MR quantitative density maps, and this corresponds with DAB-iron and CD163 across all specimens. Abbreviations: DAB, 3,3’-diaminobenzidine; MRI, magnetic resonance imaging. (For interpretation of the references to color in this figure legend, the reader is referred to the Web version of this article.)

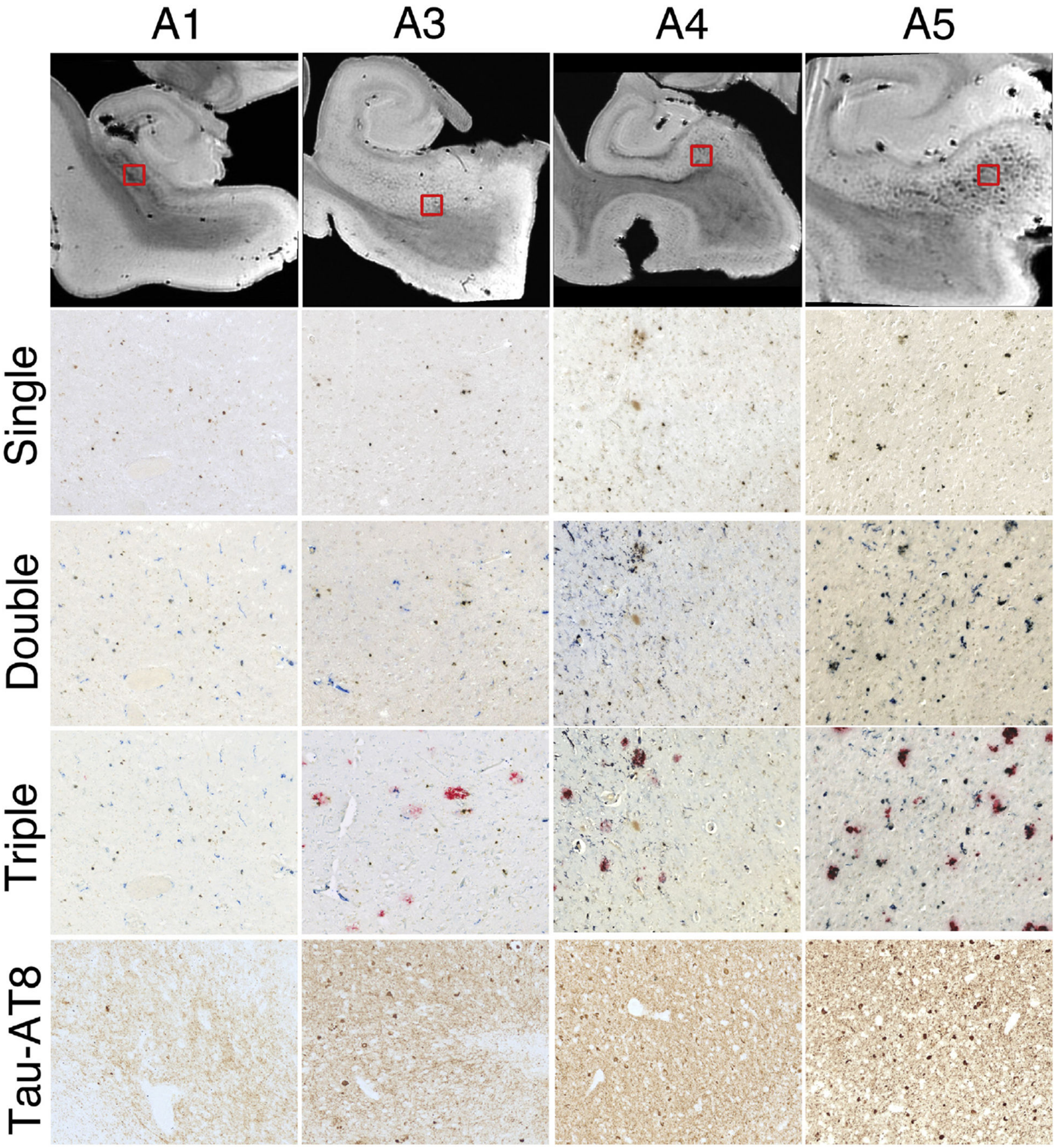

Fig. 7.

Successive histologic images demonstrating consistent iron and microglia at the subiculum. Top row: representative magnetic resonance imaging from each specimen. Successive rows: zoomed in histological sections. Single = 3,3′-diaminobenzidine (DAB)-iron (brown), double = DAB-iron (brown) plus CD163 (blue), triple = DAB-iron (brown) plus CD163 (blue) plus Aβ (red). Brightness, contrast, and color balance were adjusted homogeneously across each image to evenly emphasize iron deposits, microglia, amyloid beta (Aβ) deposits, and neurofibrillary tangles as well as neuropil threads.

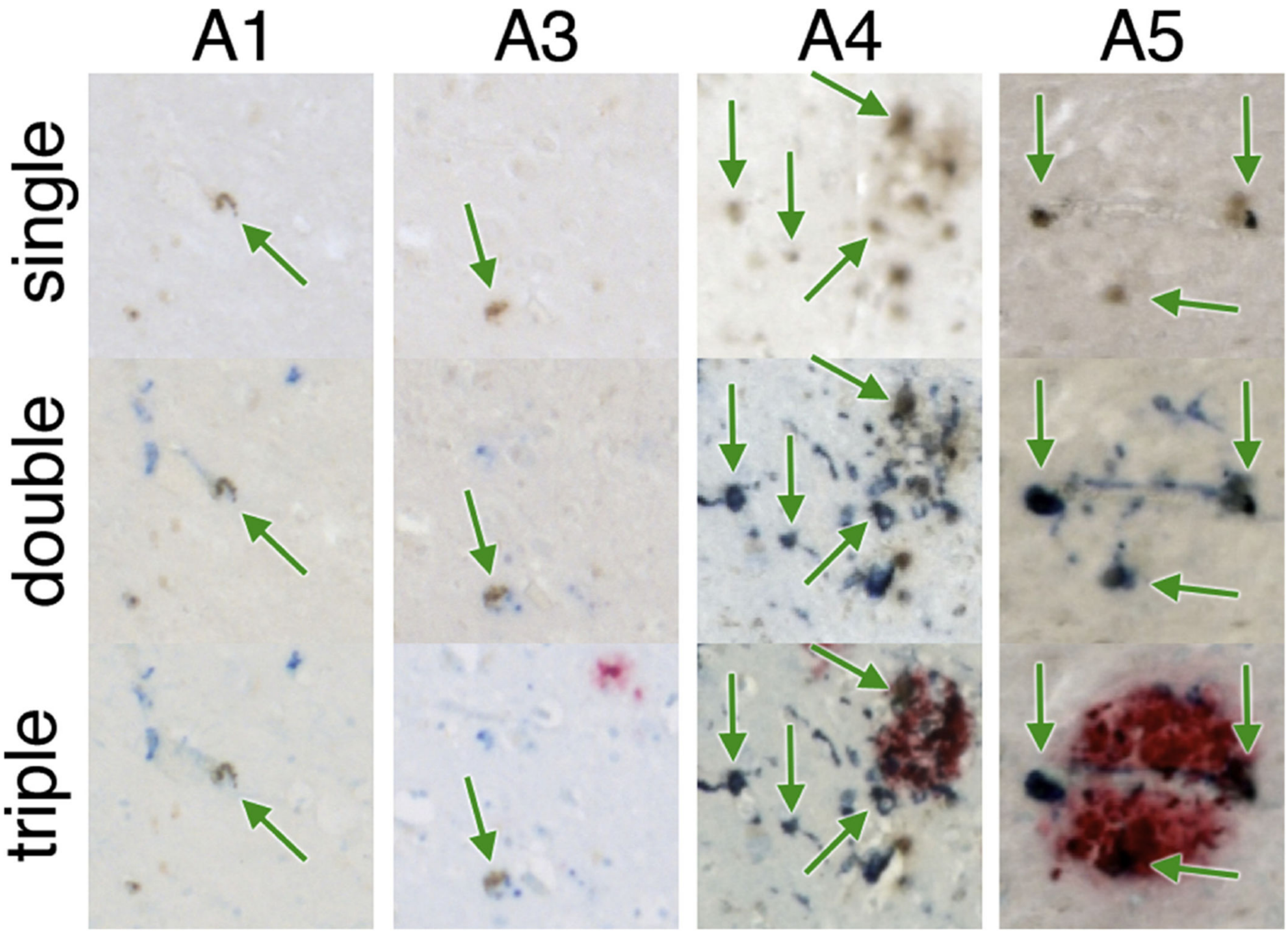

Fig. 8.

Activated, iron-containing microglia at the subiculum. Images are zoomed in from the regions of interest at the top row of Fig. 7. Single = 3,3′-diaminobenzidine (DAB)-iron (brown), double = DAB-iron (brown) plus CD163 (blue), triple = DAB-iron (brown) plus CD163 (blue) plus Aβ (red). On all slides, iron-containing microglia are evident as brown spots surrounded by blue stain, sometimes but not always associated with amyloid beta plaques. (For interpretation of the references to color in this figure legend, the reader is referred to the Web version of this article.)

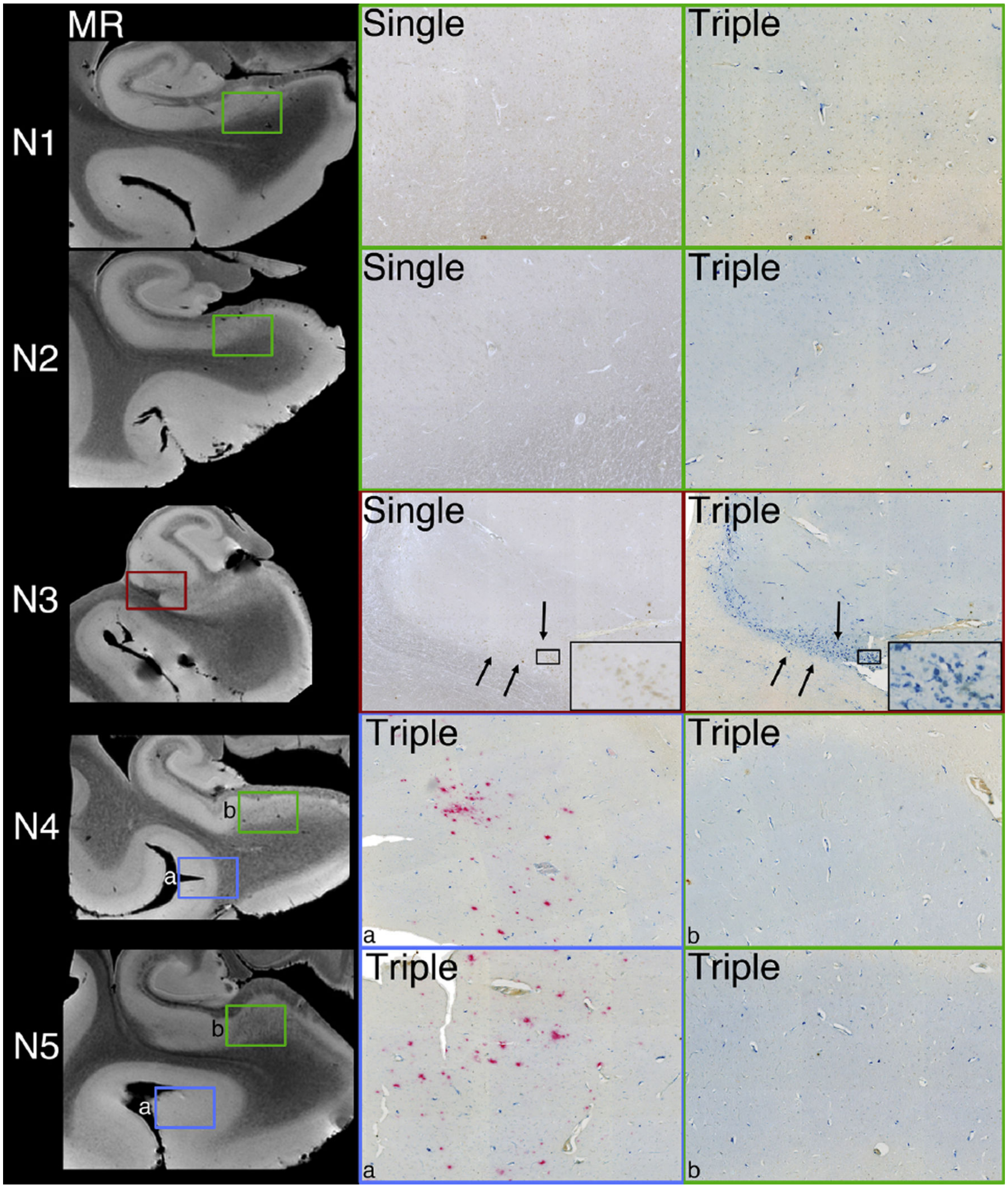

Fig. 9.

Control specimens N1–N5 MR and the associated stains for 3,3′-diaminobenzidine (DAB)-iron (brown), CD163 (blue), and amyloid beta (Aβ) (red). For N1 and N2, single (DAB-iron) and triple (DAB-iron plus CD163 plus Aβ) stains are shown zoomed into the subiculum (green boxes), where no appreciable iron, activated microglia, or Aβ are noted. N3 shows microglia at CA1 in an incidental microinfarction (red boxes, black boxes further zoomed in insets), without any appreciable adjacent Aβ deposition and significantly less iron than in the AD pathology. For N4 and N5, the blue box (a) shows a triple stain with minimal amyloid deposition in region of the medial bank of the collateral sulcus, while the green box (b) again shows the triple stains from the subiculum with no appreciable iron, activated microglia, or Aβ. (For interpretation of the references to color in this figure legend, the reader is referred to the Web version of this article.)

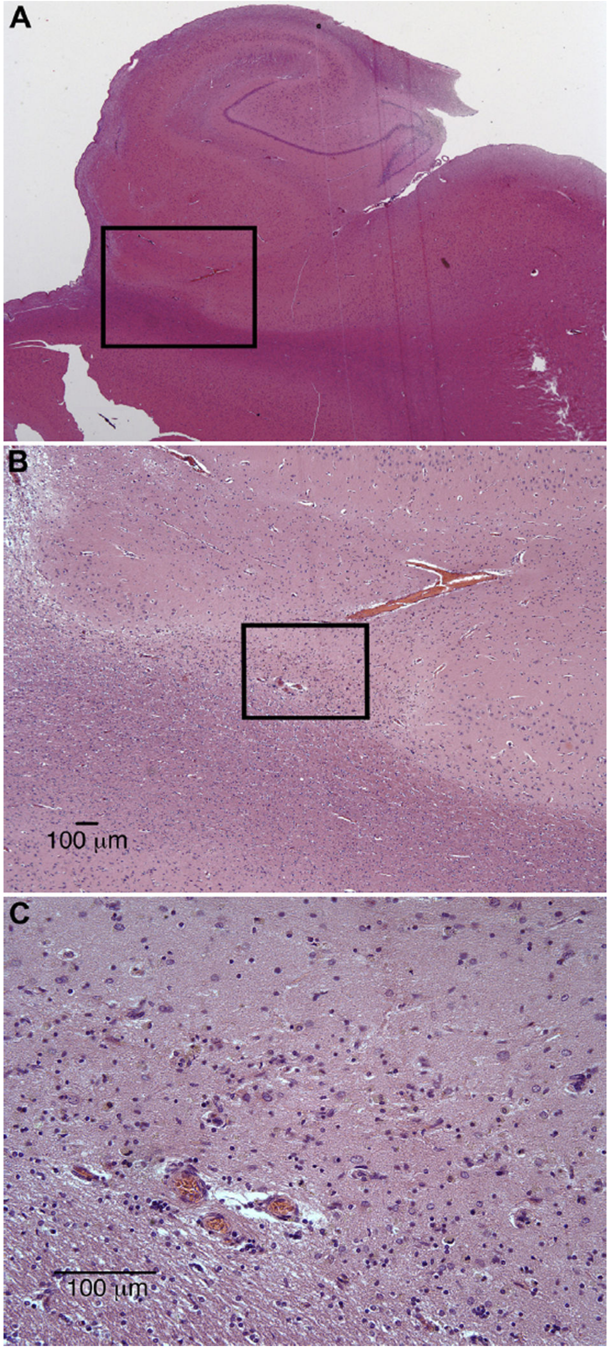

Fig. 10.

(A) Ten×, (B) 40×, and (C) 200× zoomed hematoxylin- and eosin-stained images on the incidental microinfarction in specimen N3. Neurons are absent from the infarct, and gliosis is present along with a small number of microglia.

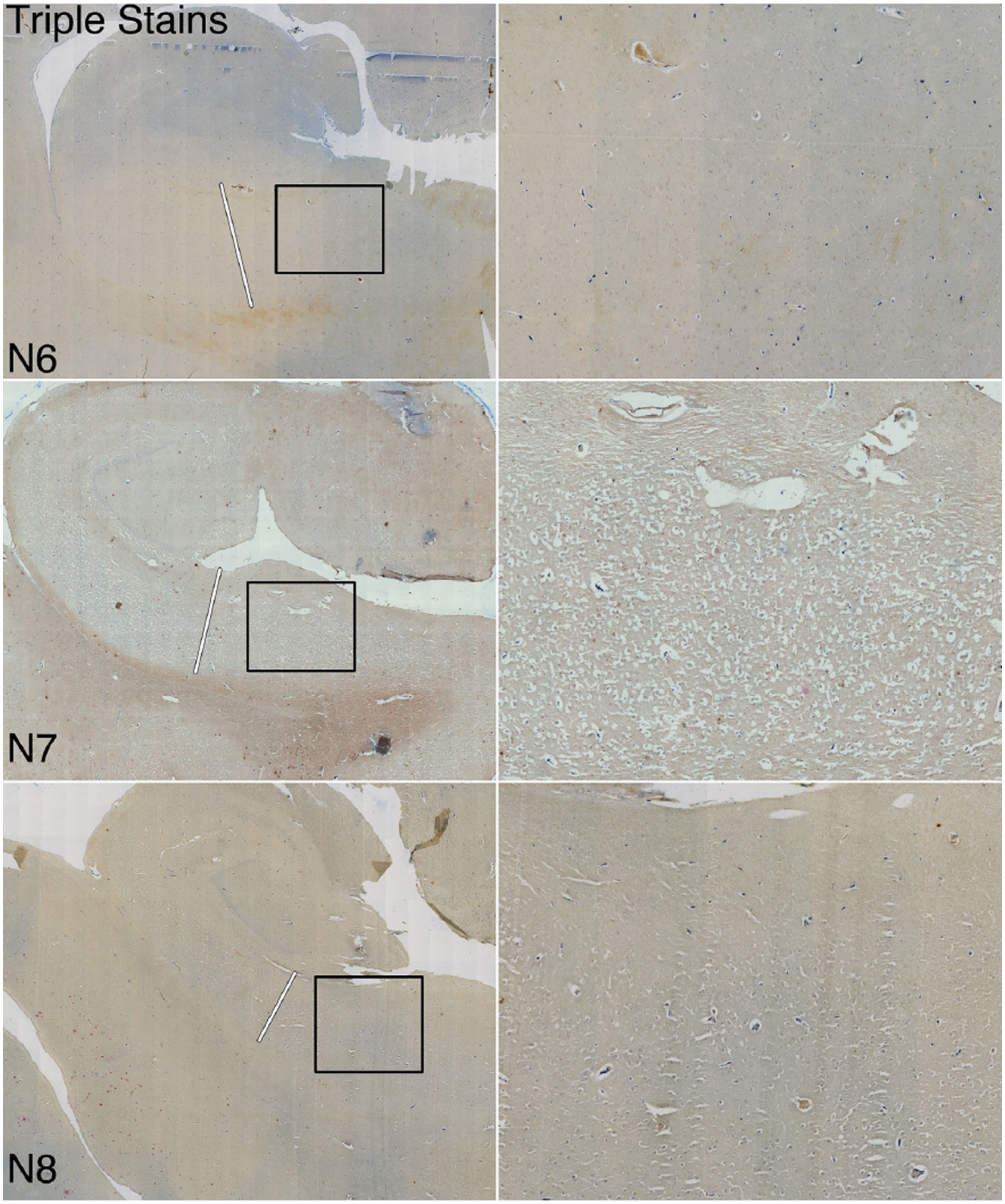

Fig. 11.

Histologic triple staining for 3,3′-diaminobenzidine (DAB)-iron, CD163, and amyloid beta on 3 additional elderly controls demonstrates the absence of iron-containing microglia in the proximal subiculum. Images were windowed and color balanced to have similar contrast.

Table 1

Pathologic data on specimens scanned

ID	Age at death	Gender	Braak and Braak stage	CERAD	Postmortem interval (h)	Secondary disease
A1	87	F	V–VI	Definite	32.48	Mild cerebrovascular disease
A2	86	F	V–VI	Definite	N/A	Cerebrovascular disease
A3	84	F	V–VI	Definite	32.52	Cerebrovascular disease
A4	89	M	V–VI	Definite	37.14	Atherosclerosis, severe
A5	83	M	V–VI	Definite	15.00	No other pathology
N1	76	F	N/A	N/A	18.14	Cerebrovascular disease
N2	68	F	N/A	N/A	6.15	Normal
N3	76	M	N/A	N/A	11.30	Normal
N4	65	F	N/A	N/A	11.30	Mild senescent changes
N5	54	M	N/A	N/A	14.90	Mild senescent changes
N6	81	F	N/A	N/A	8.44	Cerebrovascular disease
N7	76	F	N/A	N/A	19.90	Normal
N8	86	M	N/A	N/A	20.33	Cerebrovascular disease

Key: CERAD, Consortium to Establish a Registry for Alzheimer’s Disease; CVD, cerebrovascular disease; N/A, not applicable/available.

Table 2

Number of iron deposits and percentage of DAB-iron deposits that overlap with CD 163 and Aβ

	Number of DAB-iron deposits	Percentage with CD163 overlap	Percentage with Aβ overlap
A1	1817	31.0	3.5
A3	3081	35.6	9.6
A4	20,489	11.6	6.3
A5	9388	69.0	25.5

Key: Aβ, amyloid beta; DAB, 3,3′-diaminobenzidine.